Eur. Phys. J. C (2013) 73:2330
DOI 10.1140/epjc/s10052-013-2330-0

THE EUROPEAN PHYSICAL JOURNAL C

Regular Article - Experimental Physics

The GERDA experiment for the search of $0\nu\beta\beta$ decay in ^{76}Ge

K.-H. Ackermann[13], M. Agostini[14], M. Allardt[3], M. Altmann[13,b], E. Andreotti[5,18], A.M. Bakalyarov[12], M. Balata[1], I. Barabanov[10], M. Barnabé Heider[6,14,20], N. Barros[3], L. Baudis[19], C. Bauer[6], N. Becerici-Schmidt[13], E. Bellotti[7,8], S. Belogurov[11,10], S.T. Belyaev[12], G. Benato[19], A. Bettini[15,16], L. Bezrukov[10], T. Bode[14], V. Brudanin[4], R. Brugnera[15,16], D. Budjáš[14], A. Caldwell[13], C. Cattadori[8], A. Chernogorov[11], O. Chkvorets[6,21], F. Cossavella[13], A. D'Andragora[1,22], E.V. Demidova[11], A. Denisov[10], A. di Vacri[1,23], A. Domula[3], V. Egorov[4], R. Falkenstein[18], A. Ferella[19], K. Freund[18], F. Froborg[19], N. Frodyma[2], A. Gangapshev[10,6], A. Garfagnini[15,16], J. Gasparro[5,24], S. Gazzana[6,1], R. Gonzalez de Orduna[5,c], P. Grabmayr[18,a], V. Gurentsov[10], K. Gusev[12,4,14], K.K. Guthikonda[19], W. Hampel[6], A. Hegai[18], M. Heisel[6], S. Hemmer[15,16], G. Heusser[6], W. Hofmann[6], M. Hult[5], L.V. Inzhechik[10,25], L. Ioannucci[1], J. Janicskó Csáthy[14], J. Jochum[18], M. Junker[1], R. Kankanyan[6], S. Kianovsky[10], T. Kihm[6], J. Kiko[6], I.V. Kirpichnikov[11], A. Kirsch[6], A. Klimenko[4,10,6], M. Knapp[18,c], K.T. Knöpfle[6], O. Kochetov[4], V.N. Kornoukhov[11,10], K. Kröninger[13,26,27], V. Kusminov[10], M. Laubenstein[1], A. Lazzaro[14], V.I. Lebedev[12], B. Lehnert[3], D. Lenz[13,c], H. Liao[13], M. Lindner[6], I. Lippi[16], J. Liu[13,28], X. Liu[17], A. Lubashevskiy[6], B. Lubsandorzhiev[10], A.A. Machado[6], B. Majorovits[13], W. Maneschg[6], G. Marissens[5], S. Mayer[13], G. Meierhofer[18,29], I. Nemchenok[4], L. Niedermeier[18,c], S. Nisi[1], J. Oehm[6], C. O'Shaughnessy[13], L. Pandola[1], P. Peiffer[6,30], K. Pelczar[2], A. Pullia[9], S. Riboldi[9], F. Ritter[18,31], C. Rossi Alvarez[16], C. Sada[15,16], M. Salathe[6], C. Schmitt[18], S. Schönert[14], J. Schreiner[6], J. Schubert[13,c], O. Schulz[13], U. Schwan[6], B. Schwingenheuer[6], H. Seitz[13], E. Shevchik[4], M. Shirchenko[12,4], H. Simgen[6], A. Smolnikov[6], L. Stanco[16], F. Stelzer[13], H. Strecker[6], M. Tarka[19], U. Trunk[6,32], C.A. Ur[16], A.A. Vasenko[11], S. Vogt[13], O. Volynets[13], K. von Sturm[18], V. Wagner[6], M. Walter[19], A. Wegmann[6], M. Wojcik[2], E. Yanovich[10], P. Zavarise[1,33], I. Zhitnikov[4], S.V. Zhukov[12], D. Zinatulina[4], K. Zuber[3], G. Zuzel[2]

[1] INFN Laboratori Nazionali del Gran Sasso, LNGS, Assergi, Italy
[2] Institute of Physics, Jagiellonian University, Cracow, Poland
[3] Institut für Kern- und Teilchenphysik, Technische Universität Dresden, Dresden, Germany
[4] Joint Institute for Nuclear Research, Dubna, Russia
[5] Institute for Reference Materials and Measurements, Geel, Belgium
[6] Max Planck Institut für Kernphysik, Heidelberg, Germany
[7] Dipartimento di Fisica, Università Milano Bicocca, Milano, Italy
[8] INFN Milano Bicocca, Milano, Italy
[9] Dipartimento di Fisica, Università degli Studi di Milano e INFN Milano, Milano, Italy
[10] Institute for Nuclear Research of the Russian Academy of Sciences, Moscow, Russia
[11] Institute for Theoretical and Experimental Physics, Moscow, Russia
[12] National Research Centre "Kurchatov Institute", Moscow, Russia
[13] Max-Planck-Institut für Physik, München, Germany
[14] Physik Department and Excellence Cluster Universe, Technische Universität München, Munich, Germany
[15] Dipartimento di Fisica e Astronomia dell'Università di Padova, Padova, Italy
[16] INFN Padova, Padova, Italy
[17] Shanghai Jiaotong University, Shanghai, China
[18] Physikalisches Institut, Eberhard Karls Universität Tübingen, Tübingen, Germany
[19] Physik Institut der Universität Zürich, Zürich, Switzerland
[20] *Present address:* CEGEP St-Hyacinthe, Québec, Canada
[21] *Present address:* Laurentian University, Sudbury, Canada
[22] *Present address:* Brookhaven National Laboratory, Upton, NY, USA
[23] *Present address:* Department of Neurosciences and Imaging, University "G. d'Annunzio" di Chieti-Pescara, Chieti, Italy
[24] *Present address:* Nat. Physical Laboratory, Teddigton, UK
[25] *Present address:* Moscow Institute of Physics and Technology, Moscow, Russia
[26] *Present address:* II. Physikalisches Institut, U. Göttingen, Göttingen, Germany
[27] *Present address:* Department Physik, U. Siegen, Siegen, Germany
[28] *Present address:* Kavli IPMU, University of Tokyo, Tokyo, Japan
[29] *Present address:* TÜV-SÜD, München, Germany
[30] *Present address:* Karlsruhe Institute of Technology (KIT), Karlsruhe, Germany

Published online: 01 March 2013

[31] *Present address:* Robert Bosch GmbH, Reutlingen, Germany
[32] *Present address:* Photon-Science Detector Group, DESY, Hamburg, Germany
[33] *Present address:* Dipartimento di Fisica, University of L'Aquila, L'Aquila, Italy

Received: 23 November 2012 / Revised: 9 February 2013
© The Author(s) 2013. This article is published with open access at Springerlink.com

Abstract The GERDA collaboration is performing a search for neutrinoless double beta decay of ^{76}Ge with the eponymous detector. The experiment has been installed and commissioned at the Laboratori Nazionali del Gran Sasso and has started operation in November 2011. The design, construction and first operational results are described, along with detailed information from the R&D phase.

1 Introduction

The GERDA experiment (GERmanium Detector Array [1]) is a search for the neutrinoless double beta ($0\nu\beta\beta$) decay of ^{76}Ge. The observation of such a decay would prove that lepton number is not conserved, and that the neutrino has a Majorana component [2]. A discovery of $0\nu\beta\beta$ decay would have significant implications on particle physics and other fields, including cosmology [3]. The importance of the topic has stimulated the development of several experimental approaches to the search for $0\nu\beta\beta$ decay on a number of isotopes which undergo double beta decay. For recent reviews on the state of knowledge concerning double beta decay and on running or planned experiments, see Refs. [4–8].

The experimental signature for $0\nu\beta\beta$ decay is a line in the summed electron energy spectrum appearing at the Q-value for the reaction, $Q_{\beta\beta}$. The experimental result is a measurement of, or a limit on, the half life, $T_{1/2}$, for the process. Within the three neutrino model and assuming the existence of a significant Majorana component a positive observation of $0\nu\beta\beta$ decay would possibly give access to the neutrino mass hierarchy as well as information on the absolute values of the neutrino masses. The latter is only possible with knowledge of the nuclear matrix elements, $\mathcal{M}^{0\nu}$, as discussed in Ref. [9–16]. The statements on the mass also require an understanding of whether the $0\nu\beta\beta$ process is solely due to the Majorana nature of the neutrino, or whether additional new physics processes beyond the Standard Model contribute. A recent review of the particle physics implications of a discovery of $0\nu\beta\beta$ decay was given in Ref. [17].

Nuclides that are potentially $0\nu\beta\beta$ emitters will decay via the Standard Model allowed $2\nu\beta\beta$ decay. Both reactions are second order weak interactions, and therefore have extremely long half lives. Values have been directly measured for $2\nu\beta\beta$ decay in about ten cases and these are in the range 10^{19}–10^{21} yr [5]. The half lives for $0\nu\beta\beta$ decay, assuming the process exists, are expected to be substantially longer. Consequently, $0\nu\beta\beta$ decay experiments must be sensitive to just a few events per year for a source with a mass of tens to hundreds of kilograms. Backgrounds must typically be reduced to the level of one event per year in the region of interest (ROI), an energy interval of the order of the energy resolution around $Q_{\beta\beta}$.

Experiments looking for $0\nu\beta\beta$ decay of ^{76}Ge operate germanium diodes normally made from enriched material, i.e. the number of ^{76}Ge nuclei, the isotopic fraction f_{76}, is enlarged from 7.8 % to 86 % or higher. In these type of experiments, the source is equal to the detector which yields high detection efficiency. Additional advantages of this technique are the superior energy resolution of 0.2 % at $Q_{\beta\beta} = 2039$ keV compared to other searches with different isotopes and the high radiopurity of the crystal growing procedure. Disadvantages are the relatively low $Q_{\beta\beta}$ value since backgrounds typically fall with energy and the relative difficulty to scale to larger mass compared to e.g. experiments using liquids and gases. There is a considerable history to the use of ^{76}Ge for the search for $0\nu\beta\beta$ decay. After initial experiments [18–28], the Heidelberg–Moscow (HDM) collaboration [29] and IGEX [30–33] were the driving forces in this field setting the most stringent limits. In 2004 a subgroup of the HDM collaboration [34] claimed a 4σ significance for the observation of $0\nu\beta\beta$ decay with a best value of $T_{1/2} = 1.19 \cdot 10^{25}$ yr; the quoted 3σ range is $(0.69\text{–}4.19) \cdot 10^{25}$ yr. To scrutinize this result, and to push the sensitivity to much higher levels, two new ^{76}Ge experiments have been initiated: MAJORANA [35, 36] and GERDA [1]. The latter has been built in the INFN Laboratori Nazionali del Gran Sasso (LNGS) at a depth of 3500 m w.e. (water equivalent). Whereas MAJORANA further refines the background reduction techniques in the traditional approach of operating germanium detectors in vacuum, GERDA submerses bare high-purity germanium detectors enriched in ^{76}Ge into liquid argon (LAr) following a suggestion by Ref. [37]; LAr serves simultaneously as a shield against external radioactivity and as cooling medium. Phase I of the experiment is currently taking data and will continue until a sensitivity is reached which corresponds to an exposure of 15 kg yr with a background index (BI) of

[a] e-mail: grabmayr@uni-tuebingen.de
[b] Deceased
[c] Now in private business

10^{-2} cts/(keV kg yr) [1]). This will be sufficient to make a strong statement on the existence of $0\nu\beta\beta$ decay in ^{76}Ge for the best value given in Ref. [34]. Phase II of GERDA is planned to acquire an exposure of 100 kg yr at a BI of 10^{-3} cts/(keV kg yr). For pure Majorana exchange and the case that no signal is seen, this will constrain the effective neutrino mass $\langle m_{\beta\beta}\rangle$ to less than about 100 meV with the precise value depending on the choice of matrix elements [38].

The GERDA experiment is described in detail in the following sections. An overview of experimental constraints and the design is presented first. This is followed by a description of the Ge detectors. Then, the experimental setup, electronic readout, data acquisition (DAQ) and data processing are described. As GERDA Phase I has been fully commissioned and has started data production, the main characteristics of its performance are given in the final section.

2 Design and general layout

The experimental challenge is to have nearly background free conditions in the ROI around $Q_{\beta\beta}$. Typically, background levels are quoted in units of counts per keV per kilogram per year, cts/(keV kg yr), since the number of background events roughly scales with the detector mass, energy resolution and running time. Defining Δ as the width of the ROI where a signal is searched for, the expected background is the BI multiplied by Δ in keV and the exposure in kg yr. GERDA has set the goal to keep the expected background below 1 event. For $\Delta = 5$ keV and exposures mentioned above, this implies a BI of 0.01 and 0.001 cts/(keV kg yr), respectively, for the two phases of GERDA.

The main feature of the GERDA design is to operate bare Ge detectors made out of material enriched in ^{76}Ge ($^{\text{enr}}$Ge) in LAr. This design concept evolved from a proposal to operate Ge detectors in liquid nitrogen (LN_2) [37]. It allows for a significant reduction in the cladding material around the diodes and the accompanying radiation sources as compared to traditional Ge experiments. Furthermore, the background produced by interactions of cosmic rays is lower than for the traditional concepts of HDM, IGEX or MAJORANA due to the lower Z of the shielding material. Other background sources include neutrons and gammas from the decays in the rock of the underground laboratory, radioactivity in support materials, radioactive elements in the cryogenic liquid (intrinsic, such as ^{39}Ar and ^{42}Ar, as well as externally introduced, such as radon) as well as internal backgrounds in the Ge diodes. These backgrounds were considered in the design and construction phase of GERDA and resulted in specific design choices, selection of materials used and also in how detectors were handled.

Natural Ge ($^{\text{nat}}$Ge) contains about 7.8 % ^{76}Ge, and could in principle be used directly for a $0\nu\beta\beta$ decay experiment. Indeed, the first searches for $0\nu\beta\beta$ decay used natural Ge detectors [18–28]. Enriched detectors allow for a better signal-to-background ratio and also yield reduced costs for a fixed mass of ^{76}Ge in the experiment. The improvement in signal-to-background ratio originates from two sources: (i) many background sources, such as backgrounds from external gamma rays, are expected to scale with the total mass of the detector; and (ii) the cosmogenic production of ^{68}Ge and ^{60}Co in the Ge diodes occurs at a higher rate for $^{\text{nat}}$Ge than for $^{\text{enr}}$Ge. The lower overall cost is due to the fact that the high cost of enrichment is more than offset by the cost of producing the extra crystals and diodes required for $^{\text{nat}}$Ge detectors.

Figure 1 shows a model of the realized design: the core of the experiment is an array of germanium diodes suspended in strings into a cryostat filled with LAr. The LAr serves both as cooling medium and shield. The cryostat is a steel vessel with a copper lining used primarily to reduce the gamma radiation from the steel vessel. The cryostat is placed in a large water tank, that fulfills the functions of shielding the inner volumes from radiation sources within the hall, such as neutrons, as well as providing a sensitive medium for a muon veto system. A similar experimental setup has been proposed previously in Ref. [39]. The detectors are lowered into the LAr volume using a lock system located in a clean room on top of the water tank. A further muon veto system is placed on top of the clean room in order to shield the neck region of the cryostat. These installations are supported by a steel superstructure. All components are described in the subsequent sections.

Fig. 1 Artists view (Ge array not to scale) of the GERDA experiment as described in detail in the following sections: the germanium detector array (1), the LAr cryostat (2) with its internal copper shield (3) and the surrounding water tank (4) housing the Cherenkov muon veto, the GERDA building with the superstructure supporting the clean room (5) and the lock (6, design modified). Various laboratories behind the staircase include the water plant and a radon monitor, control rooms, cryogenic infrastructure and the electronics for the muon veto

2.1 Auxiliary installations

The GERDA detector laboratory (GDL), located underground at LNGS, has been used for R&D for GERDA as well as for auxiliary tests. It is a grey room equipped with a clean bench, a glove box and wet chemistry for etching. Ge diodes submerged in LN_2 or LAr can be characterized in a clean environment without any exposure to air. The detector handling described in Sect. 3 and now adopted for GERDA was developed in GDL.

The Liquid Argon Germanium (LARGE) apparatus was installed inside GDL to investigate properties of LAr, such as the scintillation light output. It is used for studies of background suppression in germanium detectors by observing the coincident scintillation light of the liquid argon [40] and to exploit the LAr scintillation light pulse shape properties to recognize the interacting particle [41]. LARGE is a 1 m^3 low-background copper cryostat with a shield consisting of (from outside to inside) 20 cm polyethylene, 23 cm steel, 10 cm lead and 15 cm copper. The inner walls are covered with a reflector foil with a wavelength shifter coating. The shifted light is detected by nine 8″ ETL 9357 photomultiplier tubes (PMTs) from Electron Tubes Limited (ETL) [42]. Calibration sources (^{228}Th, ^{226}Ra, ^{60}Co, ^{137}Cs) have been placed in- and outside of the cryostat and the event rejection by pulse shape discrimination and scintillation light detection were studied [43]. As a consequence of these measurements GERDA decided to implement a LAr scintillation light veto for Phase II. LARGE has also been used to understand the background coming from the decay of ^{42}Ar.

In addition to GDL, screening facilities at LNGS, in particular GeMPI [44] and Gator [45], have been used extensively. Additional screening facilities have been used at different locations, including Heidelberg, Geel, and Baksan.

Finally, many of the institutes in the GERDA collaboration have laboratories which have been extensively used in R&D and testing related to the experiment.

2.2 Monte Carlo simulations

A full Monte Carlo simulation of the GERDA experiment and of many of the related R&D facilities has been setup in the form of a general and flexible framework based on GEANT4 [46, 47], which is called MAGE [48]. MAGE has been widely used for GERDA-related simulations and background studies. Conversely, most of the experimental test stands provided experimental data that were used to validate and benchmark MAGE. A detailed simulation of the LARGE setup is also available within MAGE.

A few specific GERDA-related simulations were run using other codes than MAGE. In particular, a dedicated simulation code was developed to estimate the residual background in the detector array due to external γ-rays, produced either in the surrounding rocks or in the cryostat volume [49]. The simulation code SHIELD [50] was used to optimize the shielding required for the transportation of GeO_2 enriched in ^{76}Ge from the enrichment plant to the underground storage site [51]. Neutron spectra and fluxes produced by αs from the ^{228}Th calibration sources via the (α, n) reactions were calculated through the SOURCES-4A code [52].

3 The germanium detectors

This section describes the germanium detectors that represent the core of the GERDA experiment. For Phase I all eight detectors from the former HDM and IGEX experiments [29–33] were refurbished and redeployed. For Phase II new material amounting to 50 kg $^{enr}GeO_2$ and 34 kg of $^{dep}GeO_2$ was purchased. The ^{dep}Ge, material depleted in ^{76}Ge below 0.6 %, was used to check the supply chain and methods of Phase II diode production [53]. The production and characterization of the new detectors is ongoing.

Phase I detectors are based on standard p-type HPGe detector technology from Canberra Semiconductor NV, Olen [54]. Standard closed-end coaxial detectors have a "wrap around" n^+ conductive lithium layer (∼1 mm) that is separated from the boron implanted p^+ contact by a groove; the groove region is usually passivated. The detector geometry for one of the enriched detectors is shown schematically in Fig. 2. In normal DC coupled readout, the p^+ surface (∼1 μm) is connected to a charge sensitive amplifier and the n^+ surface is biased with up to +4600 V. In the alternative readout scheme with AC coupling, the n^+ contact is grounded and the p^+ contact biased with negative high voltage (HV). The analog signal is still read out from the p^+ contact but coupled with a HV capacitor to the amplifier.

Operation of bare HPGe detectors in cryogenic liquids is a non-standard technique. The success of GERDA depends strongly on the long-term stability of the Ge detectors operated in LAr.

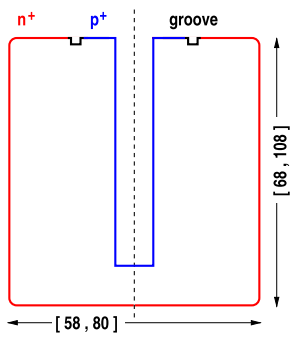

Fig. 2 Schematic drawing of a ^{enr}Ge diode currently operated in GERDA. The ranges of dimensions for the eight detectors are given in units of mm. The masses range from 0.98 to 2.9 kg

3.1 Prototype detector testing in LAr and in LN_2

Before deploying the enriched detectors in LAr, bare ^{nat}Ge detectors built with the same technology as the Phase I detectors were used for tests in GDL. A long-term study of the leakage current (LC) of bare detectors operated in LN_2 and LAr under varying γ-irradiation conditions was performed. Irradiation of a first prototype detector in LAr with γ's resulted in a continuous increase of the LC (see Fig. 3, left).

The ionizing radiation created the expected bulk current in the detector ($\sim$40 pA), observed as a step at the start of the γ-irradiation at $t \sim 2$ d. This was then followed by a continuous increase of the LC. After about one day of irradiation, at $t \sim 3.5$ d, the source was removed and the LC stabilized at a higher value than prior to the irradiation (ΔLC $\approx$ 30 pA). No increase of the LC was observed with the same detector assembly in LN_2 after one week of irradiation.

The process is reversible as the LC was partly restored by irradiation with the same source but without applying HV; the LC was completely restored to its initial value by warming up the detector in methanol baths. These measurements are the first observation of γ-radiation induced leakage current increase for detectors of this design operated in this way. The γ-radiation induced LC was measured for different HV bias values, source-detector configurations and HV polarities [55, 56]. Measurements with three prototype detectors using different sizes of groove passivation (large area, reduced and none) were performed. It was found that reducing the size of the passivation layer strongly suppresses the γ-radiation induced LC (see Fig. 3, right). The most likely explanation is that the LC increase is induced by the collection and trapping of charges produced by the ionization of LAr on the passivated surface of the detector. No γ-radiation induced LC increase was observed with the prototype without passivation layer.

For all stability measurements [56], the detectors were biased above their nominal operation voltage. The LC, continuously monitored with high accuracy, was at a few tens of pA for each detector, similar to the values measured at the detector manufacturer. Detectors with no passivation layer showed the best performance in LAr. Consequently, all GERDA Phase I detectors were reprocessed without the evaporation of a passivation layer. Our positive results on the long-term stability of Ge detectors in LAr and LN_2 contradict the statements made in Ref. [57].

3.2 Phase I detectors

The enriched Phase I detectors ANG 1-5 from the HDM and RG 1-3 from the IGEX collaborations were originally produced by ORTEC. In addition, six detectors made of ^{nat}Ge are available from the GENIUS-TF experiment [58, 59]. They have been stored underground and therefore their intrinsic activity is low. Thus, they have been used in the commissioning phase of GERDA. Details of the characterization of the enriched detectors before they were dismounted from vacuum cryostats in 2006 are reported in Ref. [60].

The Phase I detectors, ^{enr}Ge and ^{nat}Ge, were modified at Canberra, Olen [54], in the period from 2006 to 2008. The detector ANG 1 had a previous reprocessing at the same manufacturer in 1991. The work was performed according to the standard manufacturer technology, however the passivation layer on the groove was omitted. Leakage current and capacitance of each detector were measured in LN_2 at the manufacturer site after the reprocessing [56].

The detector dimensions after the reprocessing, the operating bias determined in the LAr test bench of GDL and with the abundance of ^{76}Ge measured earlier are reported in Table 1. A total of $\sim$300 g was removed from the detectors

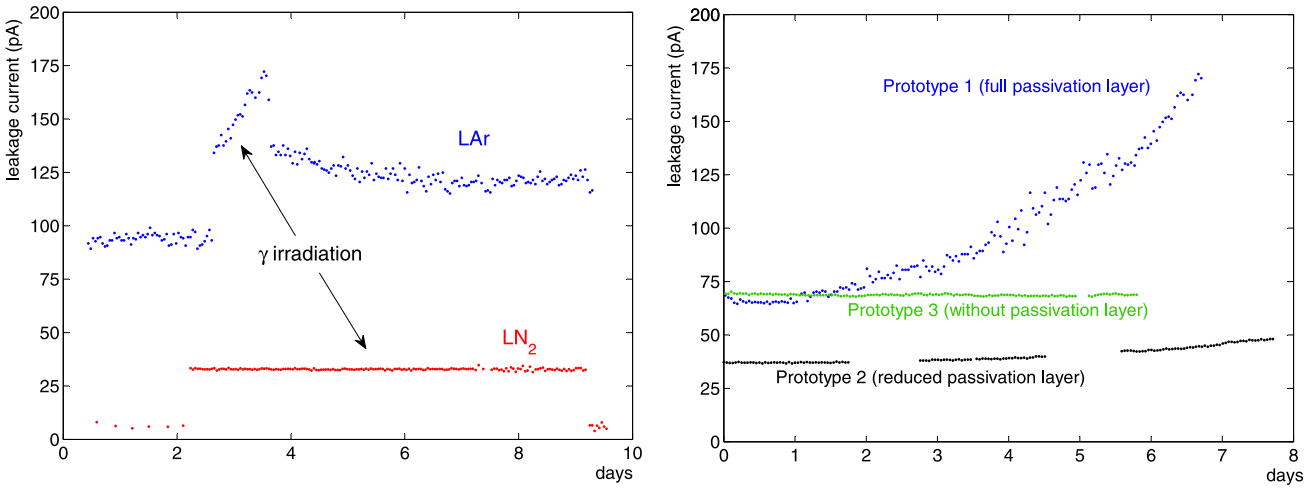

Fig. 3 *Left*: γ-radiation induced leakage current (LC) of the first prototype operated in LAr. *Right*: γ-radiation induced LC for 3 prototype detectors with different passivation layers

Table 1 Characteristics of the Phase I enriched and natural detectors. The isotopic abundances for ^{76}Ge, f_{76}, of the ANG-type detectors are taken from Ref. [62]; those for RG-type detectors are from Ref. [63]; the natural abundance [64] is taken for GTF detectors. The numbers in parentheses in the last column give the 1σ-uncertainties (for details see Table 2)

detector name	serial nr. ORTEC	diam. (mm)	length (mm)	total mass (g)	operat. bias (V)	abundance f_{76}
ANG 1	⋆	58.5	68	958	3200	0.859 (13)
ANG 2	P40239A	80	107	2833	3500	0.866 (25)
ANG 3	P40270A	78	93	2391	3200	0.883 (26)
ANG 4	P40368A	75	100	2372	3200	0.863 (13)
ANG 5	P40496A	78.5	105	2746	1800	0.856 (13)
RG 1†	28005-S	77.5	84	2110	4600	0.8551 (10)
RG 2†	28006-S	77.5	84	2166	4500	0.8551 (10)
RG 3†	28007-S	79	81	2087	3300	0.8551 (10)
GTF 32	P41032A	89	71	2321	3500	0.078 (1)
GTF 42	P41042A	85	82.5	2467	3000	0.078 (1)
GTF 44	P41044A	84	84	2465	3500	0.078 (1)
GTF 45	P41045A	87	75	2312	4000	0.078 (1)
GTF 110	P41110A	84	105	3046	3000	0.078 (1)
GTF 112	P41112A	85	100	2965	3000	0.078 (1)

⋆Produced by Canberra, serial nr. b 89002

†As different types of measurements vary, an uncertainty of 2 % is taken in evaluations

during reprocessing resulting in 17.7 kg enriched diodes for Phase I. The active masses of the detectors were assessed at typically ∼87 % by comparing γ-ray detection efficiencies to Monte Carlo simulations of the diodes with dead layer thicknesses varied [56]. This assessment will be refined with in-situ GERDA data.

Cosmogenically produced isotopes ^{68}Ge and ^{60}Co can lead to an internal contamination that represents a background in the region of interest. The detectors are always stored at an underground facility to avoid exposure to cosmic rays. This applies also for the reprocessing steps, where the detectors were stored underground at the HADES facility [61], located at a depth of about 500 m w.e. at a distance of 15 km from the detector manufacturer. The total exposure above ground was minimized to ∼5 days [56]. At the start of Phase I in November 2011, the estimated BI contribution from the cosmogenically produced ^{60}Co is on average about $(1–2) \cdot 10^{-3}$ cts/(keV kg yr). The bulk of the ^{60}Co activity comes from the production before the underground installation of the detectors for the HDM and IGEX experiments. The contribution from ^{68}Ge is negligible since it decayed away.

The mounting scheme of the detectors has competing requirements. It must have a low mass to minimize sources of radiation near to the detectors. However, the construction must be sufficiently sturdy to provide safe suspension. It must support the cables for detector bias and readout. Furthermore, the diodes must remain electrically isolated from all other materials. The chosen support design is depicted in Fig. 4 where the contacting scheme is shown as well. In order to reach the background goals of GERDA, the amount of material is minimized. Only selected high radiopurity materials were used: copper (∼80 g), PTFE (∼10 g), and silicon

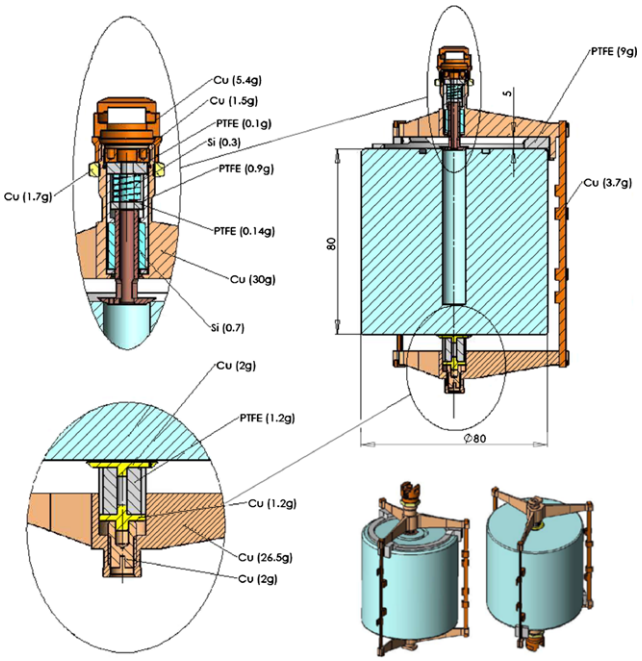

Fig. 4 Drawing of a Phase I detector assembly. The signal contact is realized by a conical copper piece ("Chinese hat") that is pushed by a silicon spring onto the p^+ contact (*inset left top*). High voltage is applied to the n^+ contact by a copper strip (not shown) pressed by a copper disc which in turn is electrically insulated by a PTFE cylinder (*inset bottom left*). The force to achieve good electrical contact is actuated through a copper screw. Masses and dimensions of the assembly are given for the RG3 detector

(∼1 g). The results of the γ ray spectroscopy measurements (see Sect. 6), combined with Monte Carlo simulations give an upper limit on the BI contribution from the detector support of $\leq 10^{-3}$ cts/(keV kg yr).

One of the prototype detectors was mounted in a support of the Phase I design to test the electrical and mechanical performance. This confirmed the mounting procedure, the mechanical stability, the signal and HV contact quality, and the spectroscopic performance of this design. During this test, the energy resolution was the same as was achieved previously when the same detector was mounted in a standard vacuum cryostat, i.e. ∼2.2 keV full width at half maximum (FWHM) at the 1332 keV spectral line of ^{60}Co.

Figure 5 shows one of the Phase I detectors before and after mounting in its custom made support structure. The Phase I detectors were mounted in their final low-mass supports in 2008 and their performance parameters (leakage current, counting efficiency, energy resolution) were measured in LAr as a function of bias voltage [56]. The detector handling was performed in GDL entirely within an environment of N_2 gas. The LC of the majority of the detectors was at the same level as measured at the detector manufacturer after reprocessing. The detectors ANG 1, ANG 3 and RG 3 showed high LCs even after successive thermal cycling and required additional reprocessing to reach an acceptable performance. Spectroscopic measurements were performed, as described in Ref. [65], with the preamplifier mounted in a gaseous Ar environment in the neck of the LAr cryostat.

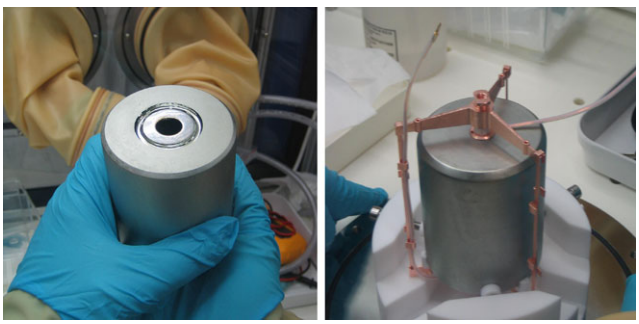

Fig. 5 *Left*: A Phase I detector after reprocessing at Canberra, Olen. The conductive lithium layer (n^+ contact) and the boron implanted bore hole (p^+ contact) are separated by a groove. *Right*: The detector is mounted upside down in a low-mass holder (groove no longer visible)

The energy resolutions of the Phase I detectors was between 2.5 and 5.1 keV (FWHM) for the 1332 keV spectral line of ^{60}Co. An improvement of the energy resolution of the detectors was observed after polishing the diode surface in the location of the HV contact.

Since November 2011 all the enriched Phase I detectors have been inserted into the GERDA cryostat.

3.3 Phase II detectors

In order to increase the active mass a new set of enriched germanium detectors is currently in production for Phase II of GERDA. A brief description of the activities is given here.

A batch of 37.5 kg of ^{enr}Ge was procured by the Electrochemical Plant (ECP) in Zhelenogorsk, Russia [66] in 2005. The isotopic content of the enriched germanium is given in Table 2. The enrichment was performed by centrifugal separation of GeF_4 gas, and the ^{enr}Ge was delivered in the form of 50 kg $^{enr}GeO_2$.

A major concern during all steps is the production of long-lived radioisotopes via cosmogenic activation, in particular ^{68}Ge and ^{60}Co. Specially designed containers were used to transport the material [51] by truck from Siberia to Germany; the $^{enr}GeO_2$ was then kept in the HADES facility in underground storage while not being processed.

A series of reduction and purification tests with ^{dep}Ge was organized. A complete test of the production chain from enrichment to the tests of working diodes was performed within a year. Based on results on isotopic dilution and yield, it was decided to further process the material at PPM Pure metal GmbH [67]. The processing of the $^{enr}GeO_2$ took place in spring 2010. The steps included a reduction of GeO_2 to "metallic" Ge, with typical purity of 3N (99.9 % Ge) and then zone refinement to 6N purity, corresponding to ≥99.9999 % chemical purity in Ge. After reduction 37.2 kg of germanium metal remained. From this material, 36.7 kg of germanium remained after zone refinement, 35.5 kg of which satisfies the 6N requirement. The biggest loss of material came from the etching of the reduced metal. The ma-

Table 2 The relative number of nuclei for the different isotopes is shown for the different detector batches. The isotopic composition of the depleted material is the average of measurements by the collaboration and ECP; that for natural germanium is given for comparison

detector batch	Ref.	germanium isotope				
		70	72	73	74	76
natural	[64]	0.204(2)	0.273(3)	0.078(1)	0.367(2)	0.078(1)
HDM–ANG 1	[73]	0.0031(2)	0.0046(19)	0.0025(8)	0.131(24)	0.859(29)
IGEX	[63]	0.0044(1)	0.0060(1)	0.0016(1)	0.1329(1)	0.8551(10)
GERDA depleted		0.223(8)	0.300(4)	0.083(2)	0.388(6)	0.006(2)
GERDA Phase II ⋆	[66]	0.0002(1)	0.0007(3)	0.0016(2)	0.124(4)	0.874(5)
MAJORANA	[74]	0.00006	0.00011	0.0003	0.0865	0.914

⋆Numbers in brackets represent the range of measurements from ECP

terial was stored in a mining museum near PPM between processing steps.

For further processing the material was shipped in a special container to Canberra, Oak Ridge [68]. Zone refining to 11N and pulling crystals of the required dimensions with a net carrier concentration corresponding to 12N purity and other characteristics such as crystal dislocation density within a specified range [69] has been completed there. The crystals have been cut and 30 slices have been brought to Canberra, Olen, for detector production. The total mass of the slices amounts to 20.8 kg.

The new detectors are of Broad Energy Germanium (BEGe) [70] type with good pulse shape discrimination properties [71, 72]. The first seven have been produced and tested in vacuum cryostats reaching a (mean) energy resolution of 1.7 keV FWHM at the 1332 keV ^{60}Co line. Five of them have been placed into a string and inserted into the GERDA cryostat in July 2011. Given the environmental electromagnetic noise of the GERDA infrastructure the resolution increases to a mean of ∼3 keV FWHM.

4 Experimental setup

GERDA occupies an area of 10.5 × 10.4 m^2 in Hall A of LNGS between the TIR tunnel and the LVD experiment. A model of the experiment is shown in Fig. 1. The floor area has been refurbished with reinforced concrete for enhanced integral stability and was sealed with epoxy for water tightness. A grid surrounding the water tank is connected to the new LNGS water collection system. The various components were erected sequentially. The construction of the bottom plate of the water tank (Sect. 4.2) was followed by the installation of the cryostat (Sect. 4.1) which arrived by a flat-bed truck from the manufacturer in March 2008. After the acceptance tests, the water tank construction was resumed and finished in June 2008. Subsequently the GERDA building (Sect. 4.3) was built and on top of it the clean room (Sect. 4.4) was erected; the latter houses the lock system with a glove box, the calibration system (Sect. 4.5) as well as auxiliary cabinets. The earthquake tolerance of the setup was verified by calculating the relative motions of cryostat, water tank and GERDA building for a seismic event with strength and frequency parameters provided by LNGS. The muon veto system (Sect. 4.6) consists of two parts, the water Cherenkov detector which is mounted within the water tank and an array of plastic scintillators which are located on the roof of the clean room.

4.1 The cryostat and its cryogenic system

The GERDA cryostat holds 64 m^3 of LAr which serves as medium for the cryogenic operation of the bare Ge diodes as well as a shield against the remnants of the external γ background penetrating the surrounding water and against the radioactivity of the cryostat itself. Leakage of radon from the atmosphere into the cryostat is prevented by the exclusive use of metal seals in the joints and valves and by keeping an overpressure of about $3 \cdot 10^4$ Pa against atmosphere. In the original design copper of low radioactivity, i.e. <20 μBq/kg of ^{228}Th, was foreseen as production material. However, safety issues and an unexpected cost increase forced the change to a stainless steel cryostat with an internal copper shield. Taking into account the measured radioactivity values of the stainless steel material [75] (see Sect. 6), the thickness of the copper shield was determined by analytical calculations and MC simulations such that sources of γ radiation external to the cryostat and the cryostat itself contribute to the BI by about $0.5 \cdot 10^{-4}$ cts/(keV kg yr) [49].

This section describes the cryostat and the cryogenic system required for its stable operation and some performance features of the setup. At the end special safety aspects are discussed that result from the operation of a cryostat immersed into a large water volume located in an underground site.

4.1.1 The cryostat

The cross section of the super-insulated cryostat is shown in Fig. 6. The cryostat is supported by a skirt (item 1) at a height of about 1.3 m above the bottom of the water tank. Access to the volume below the cryostat within the skirt is provided by two manholes (item 2). The cryostat consists of two coaxial vessels comprising of torospherical heads of 4200 and 4000 mm outer diameter and corresponding cylindrical shells of about 4 m height. The inner vessel rests on eight Torlon [76] pads (item 3) located on the bottom head of the outer vessel. Both vessels have a cylindrical neck of 1.7 m height and are connected at the top. The compensation for thermal shrinkage of the inner container is provided by a double-walled stainless steel bellow in its neck (item 7). In the upper region the outer neck carries four DN200 flanges (item 9) which are protected against the water by a kind of "balcony" surrounding the neck (item 8). A flexible rubber fabric closes the gap between the water tank roof and the balcony. The flanges allow access to the volume between inner and outer vessel and they carry the pump and the pressure sensors for the insulation vacuum as well as a safety disc as protection against overpressure. The neck of the inner vessel with an inner diameter of 800 mm provides the only access to the interior of the cryostat. A manifold (item 10) on top of the neck carries the flanges for the feedthroughs of all devices that penetrate into the cold volume including a filling tube, gas exhaust tube, tubes for active cooling, and feedthroughs for the cryostat instrumentation. The Ge diodes are lowered into the cryostat through a lock which

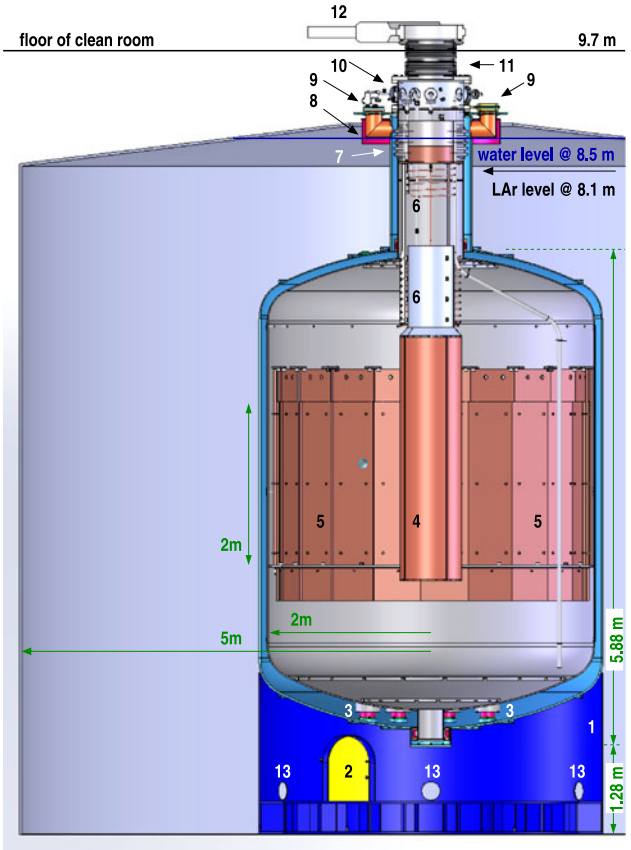

Fig. 6 Cross section of the LAr cryostat inside the water tank (right part cut away). The following components are indicated: skirt (1), access hole (2), Torlon support pads (3), radon shroud (4), internal copper shield (5), lower and upper heat exchanger (6), bellow in neck of inner vessel (7), balcony (8), DN200 ports (9), manifold (10), bellow between cryostat and lock (11) and DN630 shutter (12). The skirt provides 6 mounts for PMTs (13)

resides in the clean room above the manifold (see Sect. 4.4). Relative movements between manifold and lock are decoupled from each other with a flexible bellow of 600 mm diameter (item 11). A DN630 UHV shutter (item 12) on top of the bellow allows the stand-alone operation of the cryostat without lock.

The internal copper shield (item 5) consists of sixty 3 cm thick overlapping plates of high purity oxygen free radiopure (OFRP) copper with a total mass of 16 t. They are mounted on a support ring achieving a copper thickness of 6 cm for the central 2 m high ring (centered at 4 m height) and of 3 cm thickness in a range of 40 cm above and below.

Radon can emanate from the vessel walls and may be transported by convection close to the Ge diodes. To prevent this a central volume of about 3 m height and 750 mm diameter is separated from the rest by a cylinder (item 4) made out of 30 μm thick copper foil. This cylinder is called the radon shroud.

During production and after its deployment at LNGS the cryostat has been subjected to several acceptance and performance tests. Both the inner and the outer vessel passed the pressure vessel tests according to the European pressure vessel code PED 97/23/EC. Helium leak tests for the inner and the outer vessel showed no leak at the 10^{-5} (Pa ℓ)/s range. Evaporation tests with LN_2 established the specified thermal loss of <300 W both at the factory and after delivery. The ^{222}Rn emanation rate of the inner volume of the cryostat has been measured at room temperature at several stages with the MoREx system [77] (for details see Table 4 in Sect. 6.2). After iterated cleaning the empty cryostat exhibited the excellent value of (14 ± 4) mBq which increased after the mounting of the Cu shield and the cryogenic instrumentation by about 20 mBq at each step, leading to a final value of (54.7 ± 3.5) mBq. A uniform distribution of this amount of ^{222}Rn in the LAr would correspond to a BI $\sim 7 \cdot 10^{-4}$ cts/(keV kg yr). Depending on its tightness, the radon shroud is expected to reduce this contribution by up to a factor of seven.

4.1.2 *Cryogenic system*

The cryogenic infrastructure consists of storage tanks, super-insulated piping, and the systems for vacuum insulation, active cooling, process control, and exhaust gas heating. The power for the entire system is taken from a dedicated line which is backed-up by the LNGS diesel rotary uninterruptible power supply.

The storage tanks for LN_2 and LAr, about 6 m^3 each, are located at about 30 m distance. To minimize argon losses they are connected by a triaxial super-insulated pipe (LAr, LN_2 and vacuum super-insulation from inside to outside) to the cryostat. The LAr tank has been selected for low radon emanation. The tank has been used for the filling of the cryostat and will be used further for optional refillings. The LAr passes through a LN_2-cooled filter filled with synthetic charcoal [78] to retain radon as well as through two PTFE filters with 50 nm pore size to retain particles. For the first filling the charcoal filter was bypassed.

The insulation vacuum has to be maintained in a volume of about 8 m^3. Out-gassing materials in this volume include about 75 m^2 of multilayer insulation and 50 m^2 of additional thermal insulation (Makrolon [79] of 6 mm thickness). A pressure of 10^{-3} Pa was reached after two months of pumping with a turbo pump of 550 ℓ/s pumping speed and intermediate purging with dry nitrogen. After cool down the pressure dropped to about $2 \cdot 10^{-6}$ Pa. At a residual outgassing rate in the range of 10^{-5} (Pa ℓ)/s, the turbo pump is kept running continuously.

The active cooling system uses LN_2 as cooling medium. It has been designed [80] to subcool the main LAr volume in order to minimize microphonic noise in the cryostat while maintaining a constant (adjustable) working pressure without evaporation losses. This is accomplished by two

LN_2/LAr heat exchangers (item 6 in Fig. 6), spirals of copper tube located in the main volume and at the liquid/gas surface in the neck, respectively. With the nitrogen gas pressure of $1.2 \cdot 10^5$ Pa absolute, corresponding to a LN_2 boiling temperature of 79.6 K, the LAr is cooled to about 88.8 K. Since the temperature is slightly higher than the boiling point at standard atmospheric pressure, the cryostat builds a slight overpressure until an equilibrium is reached such that no argon is lost. The daily LN_2 consumption is about 280 ℓ.

In case of an incident like the loss of insulation vacuum, LAr will evaporate at an estimated rate of up to 4.5 kg/s. The cold gas has to be heated to a temperature above 0 °C before it is discharged to the LNGS ventilation system. This is achieved by a water-gas heat exchanger (see Fig. 8) using the LNGS cooling water or the GERDA water tank reservoir.

Complete control over almost all processes is achieved with a programmable logic controller (PLC) Simatic S7 from Siemens which continuously monitors the information provided by more than 10 redundant pairs of Pt100 temperature sensors distributed in the cryostat volume, the vacuum gauges, and the level and pressure sensors. To improve the safety further pressure regulation was installed, that is independent of the PLC. The output of a stand-alone pressure gauge (SMAR LD301, [81]) regulates directly the positioner of a valve. Two such systems are implemented to further increase the reliability. All status information is communicated to the general GERDA slow control system (Sect. 5.5) and can be accessed globally via a web-based graphical user interface that also allows restricted remote control.

Since its filling with LAr in December 2009, the cryostat has remained at LAr temperature and operations have been stable. Except for a small refill of LAr during the tuning of the active cooling system and one more following a forced Ar evaporation for a radon measurement in the exhaust gas, no additional LAr refill was necessary.

4.1.3 Safety considerations

The additional risks of operating a cryostat within a water tank due to the huge latent water heat were analyzed early in the design phase. Specific mitigation measures were realized in the design, construction and the operation of the cryostat and cryogenic system. The most important ones are summarized below.

The cryostat was designed and produced according to the European pressure vessel code for a nominal overpressure of $1.5 \cdot 10^5$ Pa, even though it is operated below the limit of $0.5 \cdot 10^5$ Pa above which this code applies. An additional safety margin is provided by an increase of the wall thickness of the cold vessel by 3 mm. The risk for any leak in one of the vessel's walls is further reduced by the lack of any penetrations in the inner or outer vessel below the water fill level, the 100 % X-raying of the welds and an earthquake tolerance of 0.6 g. The use of ductile construction materials guarantees the cryostat to follow the leak-before-break principle. In case of a leak, the implementation of a passive insulation at the outside of the inner and the outer vessel will limit the evaporation rate to a tolerable maximum of about 4.5 kg/s.

The oxygen fraction in air is monitored continuously for any low level employing several units placed in the GERDA building and in the clean room. Further enhanced safety features include full redundancy of pressure and level sensors as well as the use of both a rupture disk and a safety valve for overpressure protection. The insulation vacuum is continuously monitored with a residual gas analyzer reading the partial pressures for water, argon, and nitrogen. This information will be used for diagnostics in case of an unexpected rise in total pressure. In case of a relevant leak the PLC would automatically start the drainage of the water tank. A realistic test has established the complete drainage to be possible within less than two hours (see Sect. 4.2).

4.2 The water tank and its water plant

The water tank when filled with water provides a 3 m thick water buffer around the cryostat whose purpose is fourfold: (i) to moderate and absorb neutrons, (ii) to attenuate the flux of external γ radiation, (iii) to serve as Cherenkov medium for the detection of muons crossing the experiment, and (iv) to provide a back-up for the LNGS cooling water which in case of emergency might be needed to heat the argon exhaust gas.

4.2.1 The water tank

The water tank with a nominal capacity of 590 m^3 was designed following the API 650 regulation and according to the Eurocode 8 for the design of structures for earthquake resistance. It was built completely on site after the installation of the cryostat on the pre-installed butt-welded ground plate (Fig. 7). It consists of a cylinder of 10 m diameter and 8.3 m height covered by a conically-shaped roof which extends up to 8.9 m; the water level is kept at 8.5 m. AISI 304L stainless steel was used exclusively as construction material. The sheet metal plates for the cylindrical shell have a thickness from 7 mm to 5 mm and are joined by butt welds using externally (internally) MIG (TIG) welding. An additional bottom reinforcement has been applied at the 1 foot level. Following the UNI EN 1435 code, a significant fraction of the 400 m length of welds was X-ray tested.

Access into the water tank for the installation and maintenance of the muon veto (Sect. 4.6) is possible through a manhole at the bottom of 1400×800 mm^2 size. The roof has a central hole of 1200 mm diameter through which the neck of the cryostat sticks out. The gap between neck and

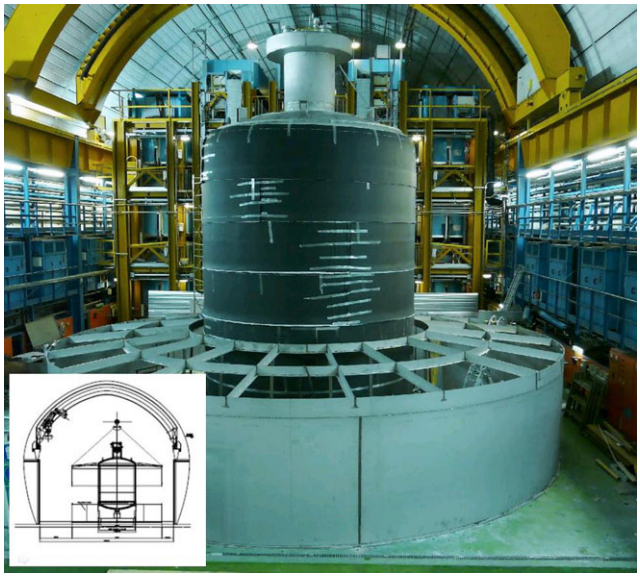

Fig. 7 The water tank under construction in Hall A of LNGS in front of the LVD detector. The *inset* shows how the tank is assembled from top to bottom. The hall crane lifts the upper part to which another cylinder segment of about 2 m height is welded. The cryostat in the center is protected by a black foamed plastic during the construction of the water tank

the roof is closed by a flexible membrane made of rubber to block radon and light from the water volume. Radon intrusion is further reduced by a slightly over-pressurized nitrogen blanket between water and roof. Besides numerous small flanges, the water tank has a further DN600 manhole as well as a DN600 chimney for the PMT cables on the roof, and, at the bottom, two DN300 flanges for fast water drainage.

The water tank was filled via a dedicated pipeline from the Borexino plant [82, 83] with ultrapure water of resistivity close to the physical limit of 0.18 MΩ m. The static test of the water tank consisted in the measurement of its radial deformation of the tank as function of the water column height and finally applying an overpressure of 10^4 Pa. Radial deformations were measured in three azimuthal locations at a height of 1 m and in one location at a height of 4 m. The maximum deformation was 7 to 8 mm as measured both in the azimuth of the manhole at 1 m height and on the opposite side of the tank at 4 m height. The deformations were proven to be elastic.

The water tank exhibits various features to ensure safe operation (see Fig. 8). A pressure relief valve will open when the nominal overpressure of $(2–3) \cdot 10^3$ Pa is exceeded. Complete drainage of the water was demonstrated in less than two hours. A constant drainage rate through a new DN250 pipe underneath the TIR tunnel of up to 65 ℓ/s is controlled by the PLC. According to the actual water level, the PLC sets the opening angle of a butterfly valve on that pipe to control the rate. A second pipe, with a maximum flow rate of 16 ℓ/s, leads via the grid to the Hall A pits that are devoted to collecting any fluid accidentally discharged by the experiments. In an emergency, a third channel is opened to pump water from the water tank at a rate of 20 ℓ/s through the heater for the LAr exhaust gas (Fig. 8). This third channel also drains to the pits in Hall A. During such an emergency event, an additional safety valve opens a vent to prevent a collapse of the water tank.

4.2.2 The water plant

The water plant (Fig. 8) has the function to keep the fraction of ions normally existing in the water, especially U, Th, K, as low as possible (fractions of ppm). Also the level of the Total Organic Carbon (TOC) must be controlled, otherwise they would cause a gradual degradation in the optical transparency of the water over time.

The water in the GERDA tank is kept in constant circulation by a loop pump at typically 3 m^3/h. In its return path the water is purified by an "Ultra-Q" unit. This is a special device equipped with four disposable cartridges containing specific resins, that removes TOC and ions (both anionic and cationic) from the water. Finally, the water is filtered for the removal of suspended particles and returned to the bottom of the water tank via a circular distribution system. The quality of the water is monitored after the filter by its resistivity and is typically higher than 0.17 MΩ m. The high light yield observed in the muon veto system (Sect. 4.6) is further proof of the excellent water quality.

4.3 The GERDA building

The GERDA building evolved from the need of a superstructure that supports a platform above the water tank and cryostat to host a clean room with the lock system for the insertion of the Ge diodes into the cryostat. The blue beams of the superstructure are visible surrounding the water tank in Fig. 1. The gap between the water tank and LVD is occupied by laboratory rooms on three levels plus a platform and a staircase. The ground floor houses the water plant and a radon monitor, the first floor two control rooms (one of them dedicated to LVD) and the second floor part of the cryogenic infrastructure including the heater for the Ar exhaust gas, safety valves and PLC as well as the electronics for the muon veto.

4.4 The clean room, twin lock and detector suspension systems

The platform on top of the GERDA building supports the infrastructure for the clean handling and deployment of the Ge detectors into the cryostat without exposing them to air.

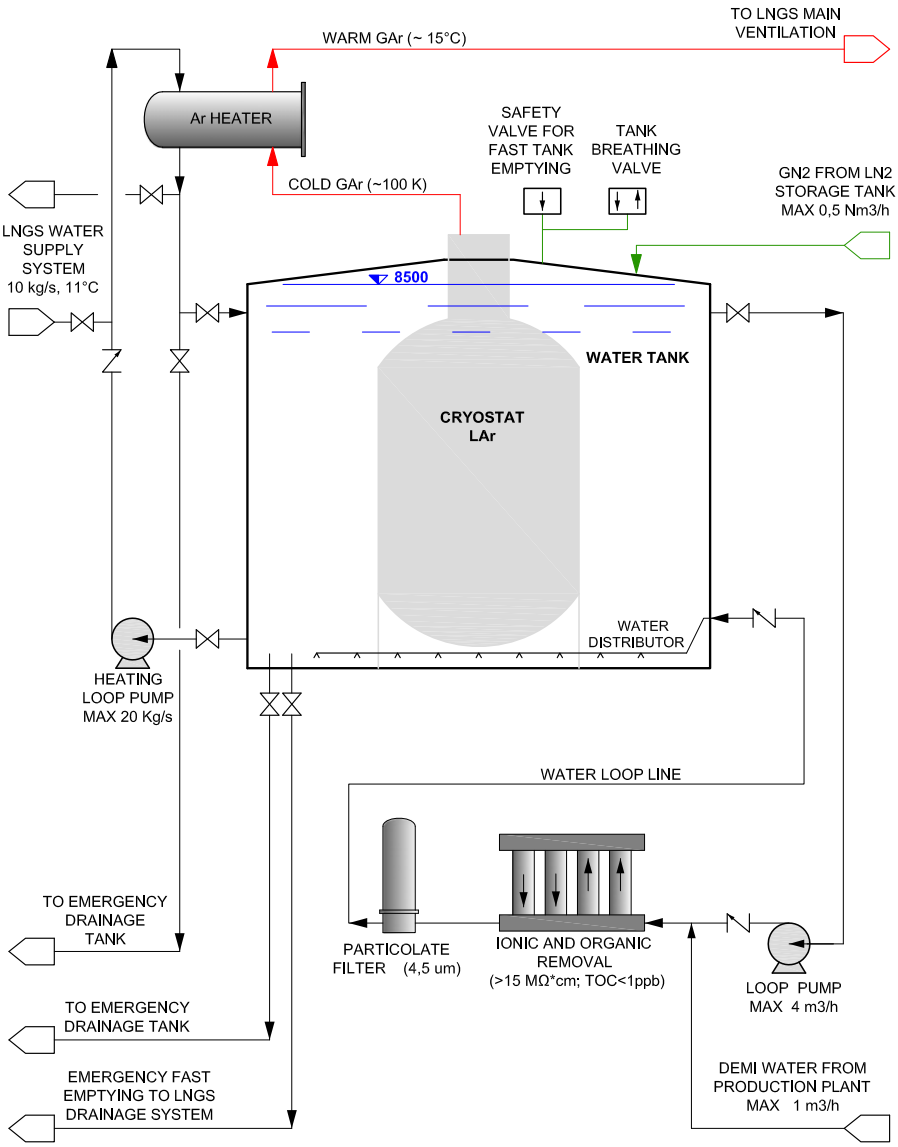

Fig. 8 Schematic of the GERDA water system including the drainage, the argon exhaust gas heater and the water plant

This infrastructure is designed as a gradient of radon reduction and cleanliness (Fig. 9). First a clean room is the working environment for experimenters within which a nitrogen flushed glove box is the working environment for the detectors. At the center a lock system provides a clean change between the environments of the glove box and the cryostat for detector insertion. The personnel lock and two small side rooms complete this complex.

4.4.1 The clean room

The clean room is a class 7 room (ISO 14644-1 [84]) corresponding to less than 10.000 particles/ft^3 of diameter $\geq$0.5 µm. An overpressure of up to 30 Pa is maintained by pressing filtered air into the clean room. The air volume of the clean room can be exchanged 49 times per hour. Access to the clean room is via a personnel lock where an overpressure of 15 Pa is maintained. The temperature inside the clean room is kept constant with variations of up to $\pm$0.3 degrees during normal operation. Maintaining the temperature within these bounds is required to prevent significant gain drifts in the electronics. The relative humidity is regulated to (50 $\pm$ 20) %. The constancy of these parameters depends to some extent on the LNGS cooling water supply of the underground laboratory.

The ceiling of the clean room follows the curved shape of the ceiling of Hall A, such that the central part of the clean room has a height of 3.6 m while the height at the wings reduces to a maximum of 2.5 m (see Fig. 9). The central part is equipped with two cranes at a height of 3.3 m that are movable along the south-north (S–N) direction, each with a maximum load of 500 kg. Both the southern wall and the central roof component are demountable. A maximum load of 150 kg/m^2 can be supported on the roof, greater than

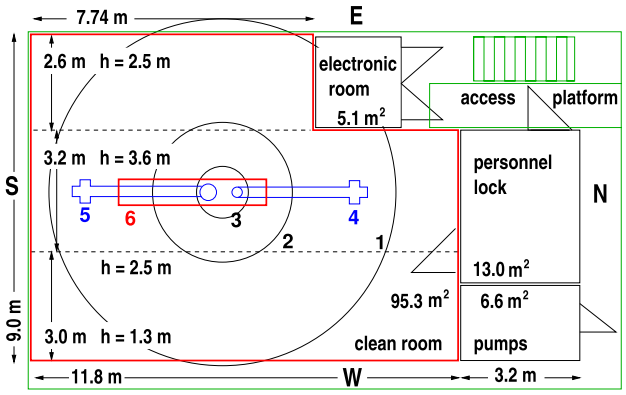

Fig. 9 Plan of the platform on top of the GERDA building showing the clean room and auxiliary cabinets. The positions of the water tank (1), the cryostat (2) and its neck (3), all below the platform, are indicated. The two arms of the lock and detector suspension system (4, 5) are connected to the cryostat. The lock is enclosed by a glove box (6). The height of the clean room varies from 1.3 to 3.6 m

the load of the plastic muon veto system (Sect. 4.6). Adjacent to the clean room is an electronic cabinet with a cable tray feedthrough to the clean room. Another adjacent room houses the pumps for the gas system of the lock.

The class 7 specifications have been met during all times while the clean room was operating. A LabView program monitors and outputs in a web interface the following parameters: particle measurements, radon content, overpressure, temperatures, and humidity.

4.4.2 *The twin lock and the suspension system*

The twin lock system for Phase I consists of two independent arms (Figs. 9 and 10) that are connected with the cryostat via a cluster flange on top of the DN630 shutter (bottom inset of Fig. 10, see also Sect. 4.1 and Fig. 6). Inside each arm is a cable chain (top inset of Fig. 10), the mechanics for lowering the detector strings into the cryostat and lights and cameras for observation during this procedure. One lock arm supports three detector strings inside a vertical tube of 250 mm diameter, while the other supports a single detector string inside a vertical tube of 160 mm diameter. Since the arms are part of the argon gas volume during data taking, they are built according to the European pressure vessel code. The locks are constructed from stainless steel tubes that are connected either by welding or by CF metal seals. The vertical section where the detector strings are mounted

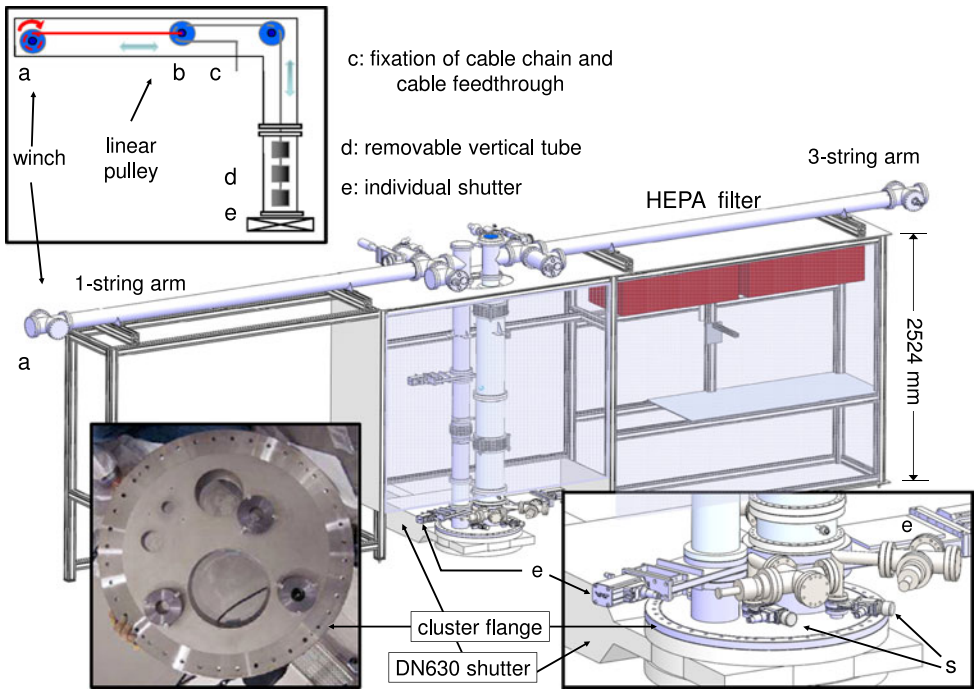

Fig. 10 Sketch of the twin lock for Phase I with its two arms on top of the DN630 shutter flange. The transparent *blue area* indicates the glove box with the HEPA filters (*red*). Each arm has an individual lock shutter (e) above which the vertical tube (d) can be removed to allow the insertion of the detector strings. The *upper inset* demonstrates the principle of the lock system: steel band (*red*) and cable chain with cables (*black*), winch (a), linear pulley (b), fixation of cable chain with cable feedthroughs (c), movable tube (d), and individual lock shutter (e). The *inset at the bottom right* details the DN630 shutter, the cluster flange, the individual tube shutters and also two of the three source insertion systems (s) above the DN40 shutters. A picture of the bottom side of the cluster flange is shown *in the bottom left*. Visible are the DN160 and DN250 openings as well as the 3 smaller openings for the sources with the tantalum absorbers (and 2 spare holes) (Color figure online)

are both located inside a glove box where HEPA filters further reduce particle concentration. Each vertical part consists of two about 1 m long tubes which exhibit the functionality of an independent lock for one or three detector strings, respectively.

Each lock arm may be closed from the cryostat by individual shutters (item e in Fig. 10) allowing for the independent operation of each when the DN630 shutter is opened. The removal of the lower part of the vertical tube (item d) allows for the insertion of detector string(s) into the lock. The Ge diodes are transferred in evacuated containers into the glove box that is purged with boil-off nitrogen gas. Within the glove box, germanium diodes and their front end electronics are assembled into strings of up to three diodes each (discussed in Sect. 5.1; a fully mounted string is shown in Fig. 17). These strings are then transferred into the lock. After the closure of the lock, it is evacuated and purged with argon gas. The two lock volumes are connected individually to a pumping station and to the cryostat through a dedicated gas system. The latter has been helium leak tested at a level of 10^{-6} (Pa ℓ)/s.

As radon can diffuse through plastic, metal seals are used almost exclusively for the lock system. All non-metal materials were screened for radon emanation (see Sect. 6, Table 5). The DN630 shutter is connected with Helicoflex metal seals, while a Kalrez seal is employed for the shutter itself. The flange with the motor axle feedthrough has a double seal EPHD O-ring. To avoid radon diffusion through this non-metal seal, the feedthrough is constantly pumped. The leak rate of the motor connection was measured to be about 10^{-5} (Pa ℓ)/s.

The scheme of the suspension system is shown in the top inset of Fig. 10. The cable chain is fixed inside the lock (item c) and runs along the 3.6 m long horizontal tube. It is deflected at the far end of the tube by 180° around the "linear pulley" (item b), a pulley that is free to move in the horizontal direction by sliding on a linear bearing. Above the cryostat the chain is deflected by 90° vertically. The linear pulley is connected to a metal band that rolls around a winch (item a) fixed to the axle of a stepper motor. By unrolling the metal band, the linear pulley moves towards the cryostat neck and the chain can be lowered into the cryostat.

The cable chain supports the detectors mechanically and provides a conduit for the signal and high voltage cables to operate them. It is constructed from stainless steel that was selected for radiopurity. Its cross section is 21×13 mm^2 with a fillable area of 17×8 mm^2. Table 3 shows the configuration of the respective cable bundles for the 1- and 3-detector string case. In the 1-string bundle all cables are wrapped in a PTFE spiral coiled tube. This protects them against damage while moving inside the cable chain during its operations. The higher number of cables needed to operate nine detectors could be accommodated only by weaving the cables with PTFE thread into flat cables and protecting them against friction with the bottom of the cable chain by a thin metal band (see Fig. 11).

The chain movement and the shutter status are controlled by a dedicated PLC. Inductive sensors are used as end switches. The position of the chain is determined redundantly by counting the number of turns of the motor and by a measuring tape with holes. An optical system counts evenly spaced holes in a steel tape that is unrolled as the chain is lowered. A friction clutch mounted between feedthrough and motor gear protects against excessive force transmission onto the cable chain.

4.5 The calibration system

Regular calibration measurements with radioactive γ sources provide the data necessary to determine the energy calibrations and resolutions of the diodes and to monitor their stability. The energy scale is tracked via monitoring of specific γ lines to identify periods in time for which single diodes showed a degraded performance. These time periods can be

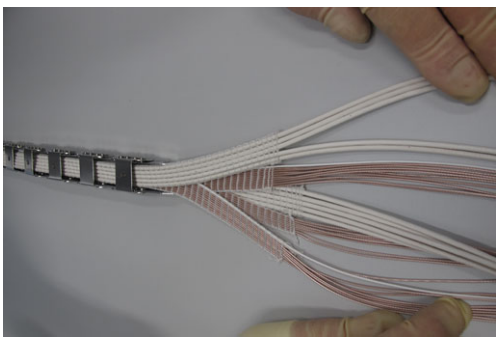

Fig. 11 Woven cable bundles in the cable chain of the 3-string lock

Table 3 Cables deployed in the 1-string and 3-string locks

cable	ref.	type	1-string	3-string
Habia SM50	[85]	50 Ω, coaxial	15	24
SAMI RG178	[86]	HV (4 kV), coaxial	4	–
Teledyne Reynolds 167-2896	[87]	HV (18 kV), coaxial	–	10
Teledyne Reynolds 167-2896	[87]	HV (5 kV), unshielded	1	2
total number			20	38

identified and omitted or specially treated in the final analysis.

In order to calibrate the detectors within the LAr cryostat, three ^{228}Th calibration sources are brought into the vicinity of the crystals. This is achieved by three vacuum sealed mechanical systems (Fig. 12) that are mounted on top of the cluster flange (Fig. 10). The systems can be individually decoupled from the cryostat via DN40 gate valves with electrical state indicators. To ensure that the background from the calibration sources is negligible during physics data taking, the sources are mounted on top of tantalum absorbers of 60 mm height and 32 mm diameter (Fig. 12). These movable absorbers rest inside the ones mounted on the cluster flange (left inset of Fig. 10). Each absorber with its source is connected to a perforated stainless steel band which is deflected by 90° before being rolled on spindles mounted behind horizontal band guides. The spindles are connected via magnetofluid sealed rotary feedthroughs to planetary geared DC motors. Friction clutches between the feedthroughs and the motors protect against excessive force transmission on the steel band. The sources are moved with a speed of 10 mm/s.

Each unit has two redundant positioning systems. An incremental encoder counts the holes of the steel band that is perforated at 4 mm pitch. The incremental encoder is mounted below the 90° deflection point at the end of the band guide. At the same position a microswitch defining the null position is mounted. A custom designed feedthrough, mounted on a CF flange, passes electronics for the incremental encoder as well as a gas line with a VCR $1/2''$ gas connection. The latter allows to pump and purge the source gas volume after the installation and before the shutter to the cryostat is opened.

The second positioning system is based on a magnetic sampling multi-turn absolute encoder with 13 bit resolution, registering changes in position even if not powered. The absolute encoder is mechanically coupled via a gear wheel to the external drive shaft on which the DC motor is mounted.

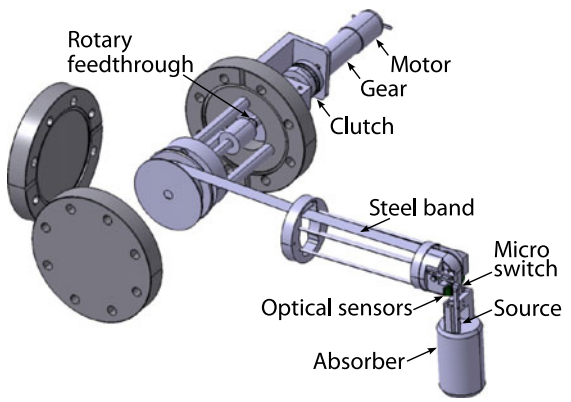

Fig. 12 A schematic view of one of three units of the calibration system (see also insets of Fig. 10 and Ref. [88])

The three source systems are controlled by a common control unit enabling the communication between a microcontroller and a PC via an RS422 interface. Each calibration source can be individually moved via a control panel displaying the actual position and status of the respective unit. The control panel also allows for a manual movement of the sources. Correction functions for the thermal contraction of the steel band immersed in the cryo-liquid are applied when calculating the position. The incremental encoder serves as the main positioning system, while the absolute encoder is calibrated with respect to it.

The RS422 interface allows to remotely control the system via a LabView GUI [89]. The GUI allows to automatize source movements, to change relevant settings, and to monitor the status of the sources and the controlling unit. A closed or undefined gate valve state vetoes any motor activity on the LabView side. Malfunctions of the systems are monitored by the micro-controller that blocks any further movement of the sources in case an error occurs.

Tests of the calibration systems prior to mounting on the cryostat showed an accuracy of the incremental encoder of ± 2 mm while the absolute encoder shows an accuracy of ± 1 mm. The position reproducibility is ± 1 mm. Tests using automatic sequencing proved that the long-term reliability of the systems is sufficient for their planned operation time. The calibration system was installed in the GERDA cryostat in June 2011. During the commissioning of a prototype system, a source dropped to the bottom of the cryostat due to the rupture of the supporting steel band. For Phase I, the resulting contribution to the BI is negligible ($\leq 1.1 \cdot 10^{-3}$ cts/(keV kg yr) based on $\sim$22 kBq in November 2011). The final version of the calibration system is working without any problems.

The energy calibration of the diodes is performed by using 7 prominent lines in the ^{228}Th spectrum: 510.8 keV, 583.2 keV, 727.3 keV, 860.6 keV, 1620.5 keV, 2103.5 keV and 2614.5 keV. For the calibration function a second order polynomial is used to account for ballistic defects of the measured pulses and for non-linearities of the electronics. Calibration spectra with the resolutions of all detectors are shown in Sect. 7.2.

4.6 The muon veto

The Gran Sasso overburden of 3500 m w.e. reduces the flux of cosmic muons to about 1.2/(h m^2) and shifts the mean energy to 270 GeV. Muons penetrating the detector will lose energy by both electromagnetic interactions and by inelastic reactions with nuclei in which high energy neutrons can be produced. These neutrons will cause inelastic interactions themselves and produce more isotopes and neutrons. Hence muons are both a direct and indirect background source.

The instrumentation of the water buffer surrounding the cryostat provides a cost-effective solution for the identification of muons by the detection of their Cherenkov light with PMTs. Muons that enter the cryostat through the neck might only pass through a small water volume. An array of plastic scintillators on the roof of the clean room provides additional covering to detect muons passing this region. Signals from both detector systems are combined as a muon veto serving the germanium DAQ. The muon veto system is designed to reduce the BI contribution from the direct muon events to a level of 10^{-5} cts/(keV kg yr) at $Q_{\beta\beta}$ in the region of interest.

4.6.1 The water Cherenkov detector

MC simulations have been used to optimize the setup and in particular to define the number of photon detectors inside the water tank [90]. A reflective foil glued on the walls of the water tank and cryostat contributes significantly to the light collection efficiency. This VM2000 foil, produced by 3M [91], has a reflectivity of >99 % over a wavelength range of 400 to 775 nm and performs well as wavelength shifter for UV light that is re-emitted in the visible spectrum. The foil has a rather small thickness of 206 µm, i.e. $\sim$0.25 kg/m^2. Almost all outer surfaces of the cryostat, the inner wall and the floor of the water tank are covered with this foil.

For the Cherenkov light detection 8″ PMTs from ETL, type 9350KB/9354KB [42], have been selected. They withstand an overpressure of $2 \cdot 10^5$ Pa absolute which is more than the pressure due to the maximum water height of 8.5 m. Since the PMTs are located outside the cryostat, there are no stringent constraints on their radioactivity. Nevertheless, 23 low-activity PMTs available were mounted in the almost closed water volume within the skirt of the cryostat (see Figs. 1 and 6) and on the bottom plate of the water tank. The selected ETL 9454KB PMTs have e.g. a potassium content reduced from 300 ppm to 60 ppm. All PMTs are encapsulated in stainless steel housings to prevent water from reaching the electrical contacts as shown in Fig. 13. In addition, the housing also acts as a mechanical support and mount for the PMTs. It consists of a steel cone, fixed to a bottom plate. To keep the PMT in position, the electrical base is fixed with polyurethane. As additional waterproofing, the electrical contacts are potted with silicone. The optical face of the housing is closed with a polyethylene terphthalate (PET) window. The volume between window and PMT is filled with mineral oil for a better matching of the refractive indices.

The electrical power for a PMT and its signal readout is provided by a single HV coaxial RG 213C/U cable with polyurethane cladding that is designed for underwater applications [92]. To facilitate timing, all cables have the same length of 35 m. In the electronics room, a splitter separates the HV and the signal lines. Extensive tests have been performed to secure the underwater tightness of the capsules. One prototype was operated at full HV inside a pressure tank for several years without degraded performance. Independent long term tests of material degradation and cable performance were also performed.

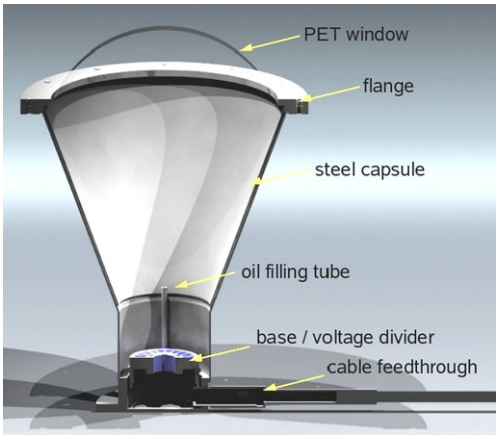

Fig. 13 Schematic drawing of the encapsulation for the PMTs of the Cherenkov muon veto. The PMT, the oil and the silicone are not shown

The water tank is equipped with 66 PMTs yielding a nominal coverage of 0.5 %. Of these, 6 are mounted on the skirt facing inwards into the volume below the cryostat. Due to the few small openings (see Fig. 6), this part is an almost independent water volume separated from the main. In the main volume, sets of 8 and 12 PMTs are mounted to the floor of the water tank facing upwards in rings of 5.5 m and 8.5 m diameter, respectively. The remaining 40 PMTs are mounted to the outer wall of the water tank facing inwards in four rings of 10 PMTs at the heights of 2 m, 3.5 m, 5 m, and 6.5 m. The high voltage is supplied via a CAEN SV1527LC crate housing 6 CAEN A1733P high voltage cards [93] with 12 positive high voltage channels each.

Five diffuser balls [94], each equipped with a single LED, are distributed throughout the water tank. When pulsed they illuminate the entire water tank volume allowing for tests of all PMTs simultaneously. The PMT gain is adjusted and the calibration, in units of photo electrons (p.e.), is made using this system. In addition, each PMT can be triggered individually through an optical fiber for calibration, monitoring, and testing [95]. The initial HV was set for a gain of $2 \cdot 10^7$ for each PMT.

4.6.2 The plastic scintillator muon veto

The second part of the muon veto system consists of 36 plastic scintillator panels located on the roof of the GERDA clean room above the neck of the cryostat. Each scintillator panel consists of a sheet of plastic scintillator UPS-923A [96] with dimensions of 200 × 50 × 3 cm^3, an attached electronics

board housing a PMT (one of 17 H6780-2 [97] or 19 PMT-85 [98]) and trigger electronics. The light produced inside the plastic panel is guided to the PMT via 56 Y11 [99] optical fibers. They are glued to both of the 200×3 cm^2 side areas of the panel.

The 36 panels are stacked in three layers with 12 modules each, covering an area of 4×3 m^2 in the N–S direction and centered at the neck of the cryostat. The panels in the second layer are placed directly on top of the first in the same orientation. The inner 8 modules of the third layer are rotated 90° degrees with respect to the lower modules to create a finer pixelization.

4.6.3 The trigger of the muon veto

The data acquisition for the muon detectors is described in Sect. 5.2.2. For a valid trigger of the Cherenkov system, at least 5 FADCs have to deliver a trigger signal within 60 ns. The threshold in each FADC channel is set such as to accept single photons with about 80 % efficiency. The Cherenkov muon veto system is running smoothly since the beginning of the commissioning runs. Three out of the 66 PMTs in the water tank have been lost during two years of operation.

A standard pulse from the Cherenkov detectors has a width of about 20 ns followed by a small overshoot and an electronic reflection around 350 ns after the main pulse. The heights of each secondary pulse was less than 1/10 of the main pulse causing no problem for the trigger system. Pulse height calibration is employed to adjust the gain of the individual PMT. At sufficient low light pulser rates the PMTs can be set to the same response by adjusting slightly the respective HV. Since September 2010 the PMTs have been checked periodically for stability. Only a few HV channels needed to be re-adjusted during that period. The single photon peak is clearly distinguishable with a peak-to-valley ratio approaching 3.

Within an event, the arrival time of pulses with a large light production is widely spread with differences up to 340 ns. Nevertheless, around half of the PMTs fire within the first 60 ns; therefore, this time interval has been chosen as coincidence time window for the trigger. The time spread is produced in part by the reflections on the VM2000 foil for the benefit of higher light yield.

As to the plastic muon veto system, the triple coincidence between the layers allows for a clear separation of γ background and muons. This is demonstrated by the spectra shown in Fig. 14. In the singles spectrum (blue), the low energy part due to γ rays is dominating and it exhibits a long tail to higher energies. The triple coincidences reveal unambiguously the minimum bias signal of muons.

The triggers of the Cherenkov and the plastic detector systems are combined via a logic OR that is recorded by the germanium DAQ.

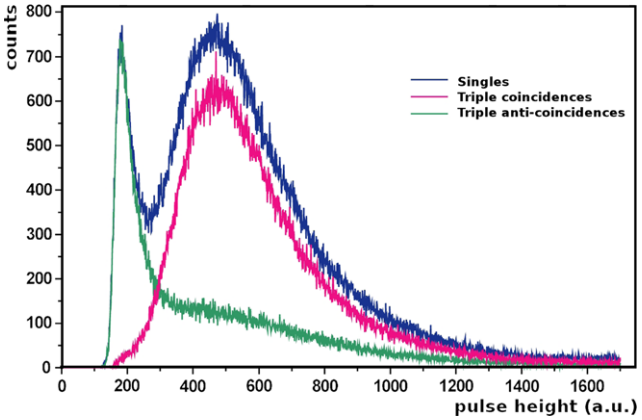

Fig. 14 Spectra taken with the plastic panels: singles (*blue*), triple coincidences (*pink*), and their difference (*green*) (Color figure online)

5 Readout, data acquisition and processing

5.1 The front-end electronics

Germanium detectors are normally read out with charge sensitive preamplifiers (CSP). In commercial devices the input transistor, a JFET, and the feedback components are close to the diode and the JFET is cooled to about 100 K for optimal noise performance. The rest of the CSP is at ambient temperature at a small distance of typically 50 cm. In GERDA, the same scheme would result in a distance of 10 m between the cold and the warm part of the CSP. The signal propagation time to close the feedback loop would consequently be longer than 100 ns. This would limit the bandwidth or lead to oscillations and the pulse shape information would be largely lost. To avoid this loss we operate the entire CSP in LAr. The minimal allowed distance between the detectors and the preamplifier depends on the radioactivity of the latter. The schematic of the implemented CSP (called CC2 [100]) is shown in Fig. 15. The input JFET is a BF862 from NXP Semiconductors and the second stage is the AD8651 from Analog Devices. Both components are used in commercial packages. Three channels are integrated on a single layer Cuflon PCB (delivered by Polyflon [101]). The feedback and test pulse capacitors are implemented as stray capacitances between traces on the PCB board (see Fig. 16). Tantalum filter capacitors are used solely and a separate line driver is omitted to limit the radioactivity (see Sect. 6.4).

The CC2 is located inside a copper box (Fig. 17, right) that provides electromagnetic shielding. The input wires connecting to the detectors are copper strips with 2×0.4 mm^2 cross section produced by wire erosion from screened material. The insulator is a PTFE tube. The same scheme is used for the last part connecting the high voltage cable to the detector. All copper strips are fixed along the detector supports to avoid microphonics.

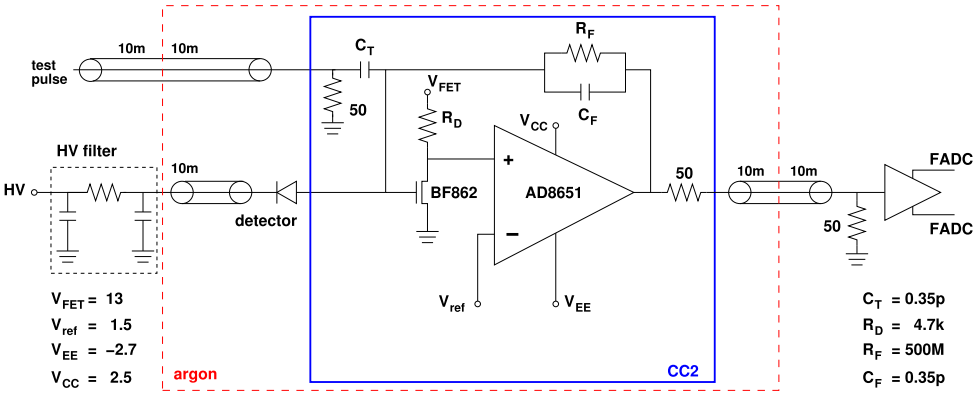

Fig. 15 The scheme of the GERDA front end circuit including grounding and cable lengths. The *parts within the dotted box* are on the CC2 PCB. The *red dashed line* shows the limits of the argon volume. The resistor values are given at room temperature (Color figure online)

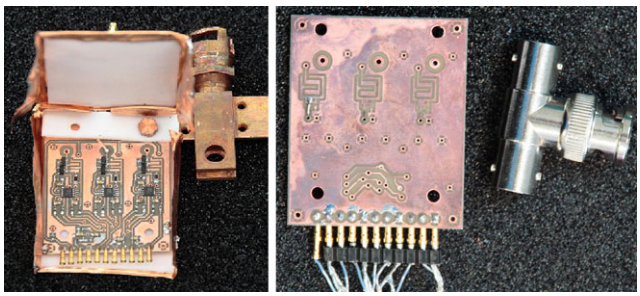

Fig. 16 The CC2 PCB front and back side integrating three channels

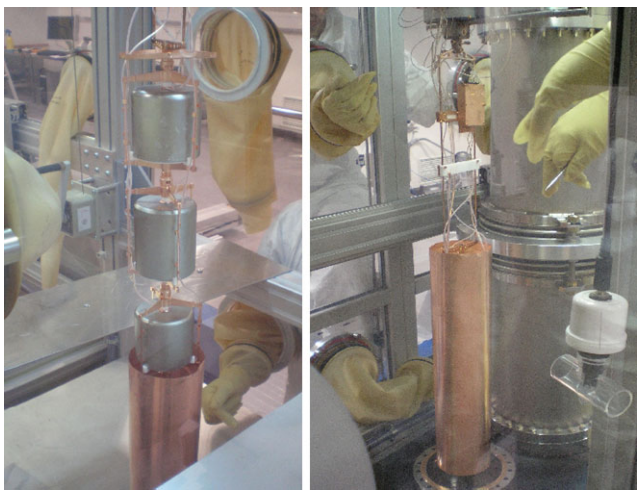

Fig. 17 *Left*: a string of three ^{enr}Ge detectors is inserted into the mini-shroud. This work is performed in the glove box of the clean room. *Right*: closed detector string and 3-channel CC2 preamplifier inside a copper box about 30 cm above the string. The connections between CC2 and detectors are made with Teflon insulated copper strips that are tightly fixed to prevent microphonics. In the background, part of the 3-string lock is visible

Realizing the CC2 with the values given in Fig. 15, its specifications are: sensitivity of 180 mV/MeV, input range at least 10 MeV, power consumption of less than 45 mW/channel, cross talk between channels of less than 0.1 %, rise time with terminated analog output of typically 55 ns, decay time of 150 µs. The noise (converted to energy equivalent FWHM for Ge) is typically 0.8 keV + 0.024 keV/pF for a 10 µs semi-Gaussian pulse shape with 8 % systematic uncertainty attached. For a 600 g coaxial detector the energy resolution achieved was 1.96 keV at the 1274 keV γ line of ^{22}Na.

A pulser signal is sent periodically to the test pulse input of the CC2 (Fig. 15). The voltage step at the capacitor C_T injects a fixed charge at the input of the CC2 and thus allows a monitoring of the entire readout chain during data taking.

Thin coaxial cables from Habia (type SM50, 94 pF/m, 0.9 Ω/m, [85]) are used for the analog outputs of the CC2 as well as for power supply (see Table 3). Welded BNC feedthroughs act as seal between air and the cryostat/lock. The ground is connected via the lock with the cryostat and water tank. RG178 cables transmit signals from the BNC connectors to the FADC in the electronics cabinet where the analog signals are digitized. The total cable length that the CC2 must drive the signal over amounts to 20 m.

The HV feedthroughs between air and the argon gas inside the lock are custom made. For leak tightness the braid of the HV cable is replaced for a few centimeters by a solid wire. The latter together with the soldered connection and part of the cable is then encapsulated with epoxy (Stycast (R) FT2850, [102]) inside a 5 cm long stainless steel pipe with a CF16 flange at one end. This solution avoids discharges in the argon gas with up to 6 kV bias on the cable. The HV cable shielding is connected to this pipe and thus also to the lock. At the air side of the feedthrough, a filter is mounted to reduce electromagnetic noise.

The HV cables inside the lock are Sami RG178 [86] and Teledyne Reynolds 167-2896 [87]. They end about 30 cm above the top detector from where the above mentioned copper strips are used. The HV bias is provided by NIM modules from CAEN (N1471H, 4ch Power Supply, [93]).

5.2 The data acquisition

The data from the Ge detectors and from the muon veto system are acquired with two different data acquisition systems.

Both systems are synchronized by a common GPS pulse per second (PPS) signal. All signals are digitized by FADCs and the energy is reconstructed offline.

5.2.1 The germanium DAQ for Phase I

The custom made Phase I DAQ [103, 104] for the germanium readout consists of NIM modules, PCI based readout boards and external logic for the trigger generation. Each NIM module digitizes 4 channels. It accepts both single-ended and differential signals. The signal polarity as well as signal attenuation (0 dB/12 dB) or gain (0-6-12-18 dB) of the analog input stage can be selected via jumpers. The offset is adjustable and the bandwidth of the anti-aliasing filter is 30 MHz. Analog-to-digital conversion is based on the Analog Devices AD6645 A/D converter (14 bits, 100 Msamples/s). The digitized data are processed with a trapezoidal filter with programmable threshold to generate a trigger, averaged to monitor the baseline and sent via an LVDS link to a PCI board. The synchronization of the different NIM modules is ensured by a common external clock and BUSY signal. The latter blocks the incoming data during readout.

The custom-made PCI readout boards are mounted in a personal computer running the Linux operating system and are operated at 32 bit/33 MHz allowing for a maximum transfer rate of 132 MB/s. Selecting a 40 µs window, four of the 10 ns samples are added (i.e. the sampling rate is reduced from 100 to 25 MHz) to reduce the data rate and readout time. For pulse shape analysis a 5 µs trace around the rising edge of the signal is stored in addition at full sampling rate. The length allows for a 10 µs shaping time for the moving window deconvolution algorithm [105], and thus no information for the energy reconstruction is lost in the compression. A 32 bit trigger counter and a 64 bit 100 MHz timestamp are saved together with the data. NIM logic builds the OR of all triggers and generates the BUSY signal.

A Qt based [106] comprehensive graphical user interface for the whole system was implemented. A JAVA-based Graphical Analysis tool was developed for online monitoring of the data. Test measurements were performed with a BEGe detector. The energy resolution was similar to the one obtained with spectroscopy amplifiers.

In addition, a copy of the hardware used for the digitization and triggering of the muon veto signals (see below) is available for the readout of the germanium detectors. Some parameters of the commercial FADCs, e.g. the shaping of the signal for the trigger, are adjusted to the preamplifier pulse shapes and the trace length is set to 160 µs. Both germanium DAQ systems are operated in parallel.

5.2.2 The muon DAQ

The muon data acquisition is installed in a VME crate housing 14 FADCs of type SIS 3301 from Struck (8 channels, 100 MHz, 14 bit, [107]). Each card has 2 memory banks of 128 k samples which are divided into 4 k size per event. If one bank is full, writing continues to the second bank while the first one can be read out. This reduces the dead time to less than 0.1 % during normal data taking. Each channel is equipped with an analog anti-aliasing filter with 30 MHz bandwidth and with a trapezoidal filter for the digitized data. If the filter output is above threshold a trigger is generated. The logical OR of all 8 triggers in a FADC module is fed into a custom made VME board, called MPIC. The MPIC generates a global trigger if a programmable number of cards output a trigger within a coincidence time window. This card also provides a time stamp for the event that is synchronized to the GPS PPS signal with 10 ns precision. If a trigger occurs, a "stop pulse" is fanned out to all FADC cards to stop writing to the circular event buffer such that the data is saved for readout. Upon a trigger, 4 µs traces for all channels are stored on disk. The stop pulse is also digitized as an additional analog input by the germanium DAQ to easily veto coincidence events. Delayed coincidences can be detected by comparing the event time stamps between the muon and germanium events in the offline analysis.

The muon veto calibration mentioned in Sect. 4.6.3 is performed by powering five LED drivers with a digital-to-analog converter (PAS9817/AO [108]) in connection with a CAEN V976 [93] fan-out for pulser signals. The light from the LEDs is uniformly distributed to all the PMTs through five diffuser balls.

5.3 Data handling

5.3.1 Data flow and blinding

The binary raw data format is defined by the different data acquisition systems. In order to optimize the analysis streaming and to provide a unique input interface for the analysis, all raw data are converted to a common standardized format. MGDO (MAJORANA-GERDA Data Objects) [109] is a software library jointly developed by GERDA and MAJORANA, that contains general-purpose interfaces and analysis tools to support the digital processing of experimental or simulated signals. The custom data objects available in the MGDO package are used as reference format to store events, waveforms, and other DAQ data (time stamps, flags). The MGDO data objects are stored as ROOT files [110]. The set of ROOT files produced by the conversion of raw data is named TIER1.

Since the information contained in the TIER1 set and in the raw data is expected to be equal, the conversion procedure is the optimal place where blinding can be applied. Events with an energy close to $Q_{\beta\beta}$ are not exported to TIER1 but they remain saved in the backup of the raw data.

The software framework GELATIO [111] contains nearly independent and customizable modules that are applied to

the input TIER1 waveforms. The results (pulse amplitude, rise time, average baseline, etc.) are stored as a new ROOT file (TIER2). A description of the analysis modules is presented in Ref. [112]. Higher level TIER*i* files can be created that contain additional parameters evaluated from more advanced analysis (e.g. calibrated energy spectra). The information of the same event stored in different TIER*i* files can be accessed by means of the ROOT friendship mechanism [110].

5.3.2 *Data storage*

The data acquisition systems store data underground on a server with 14 TB space. Every night, the newly accumulated data are transferred to a GERDA server in the LNGS computing center that has 36 TB disk space. This server is only accessible for a small number of users such that the raw data are hidden and only blinded data are available for analysis. Copies of the raw data are stored at LNGS, in Heidelberg, and Moscow.

5.3.3 *Quality control*

The event reconstruction of new data occurs automatically once per day. Since our rate is low, it is possible to store filtered information like the event energy, pulse rise time or baseline level in a data base. An interface allows simple access with a web browser or, alternatively, by a user written C++ program [113]. The event traces stored in TIER1 files can also be viewed.

A list of predefined scripts generate monitoring histograms like trigger rates versus time, pulser stability plots, baseline shifts and energy distributions and these are checked daily.

5.4 The GERDA network structure

GERDA has a dedicated network in Hall A. It is connected to the external laboratories above ground by two dedicated multi-modal optical fibers. They connect to a network switch [114] that offers access security and advanced prioritization and traffic-monitoring capabilities. The different network lines are routed inside the GERDA infrastructure.

The switch is directly connected to a dedicated server [115] that provides network routing facilities and acts as a firewall and user authentication server. At the moment, this is the only public service available directly from external networks and it is used to access all GERDA internal network resources and services. A Port Address Translation (PAT) network device is used internally, to translate TCP/UDP communications between GERDA private network computers and public network hosts.

The following centralized services are available: (i) `NIS`-server for user authentication, (ii) `DNS`-server for host name resolution, (iii) `DHCP`-server for the DAQ/slow control machines and all the computers attached temporarily to the network (i.e. laptops), and (iv) `Web`-server for the whole experiment.

In order to provide access to internal GERDA resources (mainly internal Web servers), a `proxy` service has been setup. Thus, it is possible to access internal Web servers through the main GERDA Web server.

5.5 The slow control

The GERDA slow control system [116] is responsible for:

1. monitoring of parameters characterizing the status of the subsystems (temperature, pressure, detector currents, etc.),
2. control and monitoring of low and high voltage power supplies through a graphical user interface (GUI),
3. storage of the monitored values in a database for later retrieval;
4. alarm handling,
5. web pages for subsystems breakdown,
6. online histograms for the relevant parameters,
7. reliable remote monitoring of the whole experiment.

The slow control consists of four building blocks. A database is the core of the slow control system. It stores both the data and the configurations. PostgreSQL [117] was selected as relational database SQL compliant with the capability of an embedded procedural language (PL). In case of a high number of records in the data tables, the database will be split in two: a so-called online database where all the data up to one week are stored and the historical database where older data are copied regularly after data compression.

The acquisition task is performed by a pool of clients each serving a dedicated hardware subcomponent. The clients store the acquired data in the database. Depending on the specific hardware, different types of connections are used by the clients: web access, CANbus, serial RS232, etc. All data written into the database have a proper time stamp, that constitutes the main method to study correlations. All hardware settings are stored in the database.

Alarms generated automatically by some components go directly to the LNGS safety system and to the GERDA on call experts and the slow control system will record the event into the database for future analysis. The alarm manager is a supervisor process that retrieves data from the database and is able to generate warnings or error messages in case of a malfunctioning sensor.

The system is completed by a web interface where alarms, instant and historical data (through histograms) and the status of the clients can be seen. The control interface is based on HTML. The data are updated automatically using Ajax [118] in pull manner.

The database has been operational since autumn 2009. Data collected in two and a half years are only 94 MB. This is in part due to the use of a data reduction policy at the level of the readout of some subcomponents (cryostat, clean room, water loop).

6 Summary of screening results

A very careful selection of materials is critical to achieve our goal of one to two orders of magnitude reduction in backgrounds relative to previous experiments. For Phase I, this selection was carried out by using state-of-the-art screening techniques during the design and construction phases. The screening facilities continue to be used in the preparations for Phase II of GERDA.

Material screening was performed mainly with the following three techniques:

1. Gamma ray spectroscopy with High Purity Germanium spectrometers in four underground laboratories: at the Max-Planck-Institut für Kernphysik (MPIK) in Germany, HADES (IRMM) in Belgium, the Baksan Neutrino Observatory (BNO INR RAS) in Russia and at LNGS in Italy. The ultimate detection limit for the best spectrometers in deep underground laboratories lies around 10 μBq/kg for ^{226}Ra and ^{228}Th [119, 120]. This, however, requires large sample sizes of up to several tens of kg.
2. Gas counting with ultra-low background proportional counters. They were originally developed at MPIK for the GALLEX solar neutrino experiment [121] and are used in GERDA for ^{222}Rn measurements.
3. Mass spectrometry with Inductively Coupled Plasma Mass Spectrometers (ICP-MS). The GERDA collaboration has access to two ICP-MS machines, one at LNGS and one at INR RAS, Moscow.

In addition, some dedicated samples were analyzed with Neutron Activation Analysis (NAA) and Atomic Absorption Spectroscopy (AAS).

Altogether almost 250 samples were screened by gamma ray spectroscopy. The main focus was on electronics components (about 85 samples), metal samples (about 65 samples, mostly stainless steel and copper) and plastic materials (about 50 samples). Also the Rn emanation technique was extensively applied (about 120 samples) and about 20 samples were screened by ICP-MS. In this section some selected results, most relevant to the construction, will be given. Some more results can be found in Refs. [75, 122, 123].

6.1 Argon purity

The ^{222}Rn concentration of commercial liquid nitrogen was measured [77] and its purification to a level of 1 μBq/m^3 at standard temperature and pressure has been demonstrated in the past for BOREXINO [124]. For GERDA the same questions arose for liquid argon since the ^{222}Rn concentration in freshly produced argon was found to be in the range of mBq/m^3 (STP) which is about an order of magnitude higher than for nitrogen. While this is not so relevant for the first cryostat filling, a constant refilling was considered for the case that the active cooling would fail (see Sect. 4.1.1).

Argon purification tests based on radon adsorption on low temperature activated carbon traps were performed with gaseous and liquid argon. For the gas phase, reduction factors of more than 1000 were achieved for a 150 g trap [125]. These are similar to the results achieved for nitrogen [124]. For the liquid phase, in most cases a reduction factor of 10 could be achieved for a small 60 g column. In GERDA an activated carbon column (∼1 kg) was installed, which is expected to reduce the ^{222}Rn concentration by two orders of magnitude. All measurements were performed with the Mobile Radon Extraction unit (MoREx, [124]).

6.2 Radiopurity of the cryostat

Besides the argon, the second largest mass item in close contact to the diodes is the cryostat. It is made of austenitic stainless steel with an additional inner copper shield (see Figs. 1 and 6). The stainless steel was procured in more than 10 relatively small batches of a few tons and roughly a 50 kg sample of each batch was screened with gamma ray spectrometers [75]. During this campaign it was discovered that stainless steel may have low ^{228}Th activity that is about 10 times lower than what was known from earlier screening campaigns [126]. Finally, the cylindrical part of the cryostat, closest to the diodes, could be constructed from stainless steel batches with a ^{228}Th concentration below 1 mBq/kg. All other batches have a ^{228}Th concentration below 5 mBq/kg. Another contamination in stainless steel is ^{60}Co. In the batches for GERDA, a mean ^{60}Co activity of 19 mBq/kg was found [75]. The availability of low radioactivity stainless steel led to a significant reduction in the necessary mass of the inner copper shield.

Any ^{222}Rn released from the inner surface of the cryostat will be dissolved in the liquid argon and may be transported to the germanium diodes by convection. Therefore, the ^{222}Rn emanation rate of the cryostat was measured after its construction. The cryostat was sealed, evacuated and filled with ^{222}Rn-free nitrogen gas that was produced with MoREx. After a certain time in which ^{222}Rn could accumulate, the nitrogen was agitated (to assure a homogeneous radon distribution) and a sample of a few cubic meters nitrogen was extracted. Then the ^{222}Rn concentration in this aliquot was measured with low background proportional counters and the result was scaled to calculate the ^{222}Rn emanation rate of the entire cryostat. The measurement was repeated after various modifications of the cryostat and the results are summarized in Table 4.

Table 4 Measurements on ^{222}Rn emanation of the GERDA cryostat at room temperature after various stages of construction

no.	date	description	result [mBq]
1	Nov 2007	after construction and first cleaning	23.3 ± 3.6
2	Mar 2008	after additional cleaning	13.7 ± 1.9
3	Jun 2008	after copper mounting	34.4 ± 6.0
4	Nov 2008	after wiping of inner surfaces	30.6 ± 2.4
5	Sep 2009	in final configuration	54.7 ± 3.5

The first two measurements were performed when the cryostat was still empty, i.e. just the surface of the stainless steel vessel was under investigation. The cleaning then performed was a pickling and passivation treatment with an acidic gel. In the first measurement a ^{222}Rn emanation rate of 23 mBq was measured. This reduced by a second cleaning cycle to a level of about 14 mBq. After the copper shield was installed a subsequent measurement showed an increase of the ^{222}Rn emanation rate by about 20 mBq. A plausible hypothesis was that dust was introduced during the copper mounting. However, this explanation was rejected because thorough surface wiping did not improve the result significantly (see measurement No. 4).

The final configuration of the cryostat includes a manifold through which all tubing is distributed, a compensator to connect it to the lock, a radon shroud (see Sect. 3) and many sensors and safety devices. The ^{222}Rn emanation rate of the cryostat in its final configuration is (54.7 ± 3.5) mBq. Assuming a homogeneous distribution of ^{222}Rn in the liquid argon, this would result in a contribution to the BI at $Q_{\beta\beta}$ of $7 \cdot 10^{-4}$ cts/(keV kg yr). To reduce this background, a cylinder made from 30 µm thick copper foil (called radon shroud, see item 4 in Fig. 6) was installed around the diodes with the intention that ^{222}Rn that is emanated from the walls is kept at sufficient distance from the diodes.

6.3 Radon emanation of components inside the lock

The lock system is directly connected to the GERDA cryostat (see Fig. 6 and Sect. 4.4.2). Thus, ^{222}Rn that is emanated inside the lock may be dissolved in the liquid argon and can contribute to the background. Consequently, the selection of low-emanating construction materials for the lock and items inside the lock was a rigorous process. Flanges to the outside were sealed with metal gaskets whenever possible. At places where O-rings had to be used Kalrez [127] O-rings were chosen to avoid VITON, which is known to be a relatively strong source of radon. The ^{222}Rn emanation rates of all Kalrez O-rings that are used in the lock system were investigated and it was confirmed that they are much radiopurer than VITON. As a result of these measurements, an upper limit of 0.6 mBq can be given for the integrated ^{222}Rn emanation rate of the subset of O-rings that are in direct contact with the inner volume of the lock.

Table 5 summarizes the results of all the other components in the lock that were screened for their ^{222}Rn emana-

Table 5 Radon emanation of non-metallic materials used in the lock. The amount of the material used and the corresponding emanation is listed. Values indicated by $*$ are estimated by the detection of ^{226}Ra using γ-ray screening. They are conservative upper limits since not all ^{222}Rn will escape the material

component	amount	material	total Rn emanation rate
LED	4 pieces		(207 ± 25) µBq
Kappa camera	4 pieces		<350 µBq
inductive end switch	4 pieces	mostly steel	(73 ± 13) µBq
meter drive head	2 pieces		(860 ± 180) µBq
meter drive plug	2 pieces		(400 ± 180) µBq
pulley bearings	12 pieces	Iglidur	<7.2 µBq
linear pulley guides	4 pieces	Iglidur	<4.8 µBq
O-ring seal shutter	1 piece	Kalrez	(400 ± 100) µBq
O-ring motor feedthrough	2 pieces	EPDM	(7.8 ± 1.0) µBq
HV cables SAMI RG178	40 m (300 g)		<680 µBq
signal cables Habia SM50	508 m		(273 ± 50) µBq
LV supply TR 5 kV	62 m		(50.4 ± 14.7) µBq
Thermovac pressure gauge [128]	2 pieces		<12.6 µBq
BD diff. pressure sensor [129]	3 pieces		(117 ± 18) µBq
HV cables TR 18 kV	1.53 kg (100 m)		$*$ <11.1 mBq
spiral coiled tube	273 g (11.2 m)	PTFE	$*$ <3.2 mBq

tion rate. As can be seen in the right column the integrated radon emanation rate of all components is less than 17 mBq. This is low compared to the ^{222}Rn emanation rate of the cryostat. Moreover, there are cold copper surfaces in the argon gas phase just above the liquid level which will act as a getter. Therefore, the ^{222}Rn emanation of the lock is a minor source of background for GERDA.

6.4 Further selected screening results

Before the construction of GERDA it was already known that high purity copper is one of the most radiopure materials [120]. Therefore, it was the natural candidate material for the construction of the low mass diode holder (see Table 6). As insulating material, one of the most promising candidates from previous measurements is PTFE. A batch of extruded PTFE was purchased that was produced under particularly clean conditions and screened with the GeMPI spectrometer [122].

Finally, radioactivity measurements of the GERDA front-end electronics have been performed (see Sect. 5.1). Particular efforts have been made to produce a low radioactivity version of the circuit. Some of the key points to achieve these results are: manufacturing of the printed circuit board on a specifically selected low-radioactivity substrate (Cuflon), minimization of the number of tantalum decoupling capacitors, integration of low value capacitors as stray capacitance between traces directly on board, and careful selection of passive physical components and soldering paste. To reach a BI $< 10^{-3}$ cts/(keV kg yr), the Monte Carlo predicts a maximum allowed activity for the front end electronics of 2 mBq for ^{226}Ra and 500 μBq for ^{228}Th with a separation of 30 cm between the electronics and the top detectors. The average measured activity of a set of three preamplifiers is (286 ± 28) μBq and (150 ± 24) μBq in ^{226}Ra and ^{228}Th, respectively, including the pins. Thus, the radiopurity limits are met for the 5 PCBs presently in use.

7 Performance of the apparatus

The construction of the apparatus was completed in June 2010. The commissioning phase started with the operation of refurbished ^{nat}Ge diodes from the GENIUS-TF experiment [58, 59], in order to minimize the potential risks for the ^{enr}Ge detectors. A larger background than expected at $Q_{\beta\beta}$ and an intense line at 1525 keV was discovered. The origin and mitigation was studied in the following months (see Sect. 7.3). In June 2011 a string of ^{enr}Ge diodes was deployed for further preliminary tests including various operational configurations of the detectors and the electric stray fields. The commissioning phase was completed on November 1, 2011. All components had met their design specifications and an adequate background index was reached; thus, physics data taking of Phase I was started on November 9, 2011. A blinding window of 40 keV width around $Q_{\beta\beta}$ is in place since January 11, 2012. The raw data are written to disk, however events with energies from 2019 to 2059 keV are not exported to the TIER1 data and are therefore not available for analysis. The blinding window will be opened when a sufficient exposure is acquired and the calibrations and selection cuts are finalized.

While it is not the scope of this paper to discuss the physics analysis and results, the principal performance of the apparatus is summarized here. Results are shown demonstrating that a low background has actually been reached via thorough material selection and screening. The stability of the performance of the complete GERDA setup at LNGS is inferred from the energy calibrations and the first spectra. The performance particulars are obtained on the basis of physics runs between November 2011 and May 2012, which resulted in an exposure of 6.10 kg yr for the enriched detectors and 3.17 kg yr for the natural detectors. These data are collected with an overall live time (calibration runs subtracted) of about 90 %.

7.1 The performance of the muon veto

The PMTs of the muon veto have been checked for pulse height stability for more than one year. A satisfying individual stability is reflected in the constant average light output per muon event per day (Fig. 18, squares and right scale). This constancy is mandatory for a reliable determination of the muon rate that is shown by the crosses in Fig. 18 (left scale). Except for short term fluctuation the rate is consistent with a 2 % sinusoidal variation with a period of about one year. This is a well-known phenomenon [130] that will be verified when a longer period of data is available.

The observed muon rate in GERDA results in a preliminary value of $(3.42 \pm 0.03) \cdot 10^{-4}$ cts/(m^2 s) which

Table 6 Gamma ray screening results for selected materials. Given are 1σ-boundaries or 90 % limits. Note, one PCB board serves three detectors

component	amount	^{40}K [mBq/kg]	^{226}Rn [μBq/kg]	^{228}Th [μBq/kg]
copper detector support	80 g/det.	<0.088	<16	<19
PTFE detector support	10 g/det.	0.60 ± 0.11	25 ± 9	31 ± 14
PTFE insulation pipe	2.5 g/det.	8 ± 2	1100 ± 200	<620
CC2 preamplifier	per PCB	1.8 ± 0.3	286 ± 28	150 ± 24

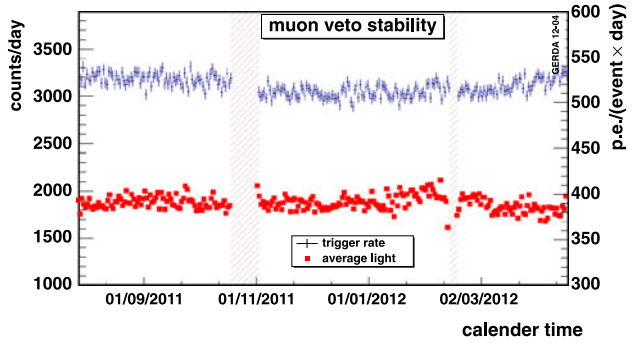

Fig. 18 The average light output per event and day (*squares, right scale*) of the Cherenkov muon veto. The daily rates (*crosses, left scale*) are rather constant

compares very well with the recent BOREXINO result of $(3.41 \pm 0.01) \cdot 10^{-4}$ cts/(m^2 s) [130].

Figure 19 shows the multiplicity M, the number of Cherenkov PMTs fired. The spectrum is taken with trigger signals from both muon veto systems with a threshold of 1 photoelectron (p.e.). The expected light yield is roughly 200 to 300 photons for every centimeter traversed by a muon. Since almost all surfaces of the water tank and cryostat are covered with the VM2000 foil, one would expect that most of the muon events will cause a high multiplicity of triggered PMTs. The low coverage of 0.5 % of the surface by PMTs is compensated by the reflectivity and wavelength shifting properties of the VM2000 foil. There is, indeed, a rise towards high multiplicities as predicted by the MC simulations, but there is also a prominent enhancement observed in the low multiplicity region below $M = 20$ which is not present in MC. The low multiplicity bump around $M = 10$ vanishes for events triggered by the plastic panels only. Therefore, it is unlikely that it is caused directly by muons. The hypothesis of local radioactivity creating scintillation light in the VM2000 foil is still investigated. Triggers

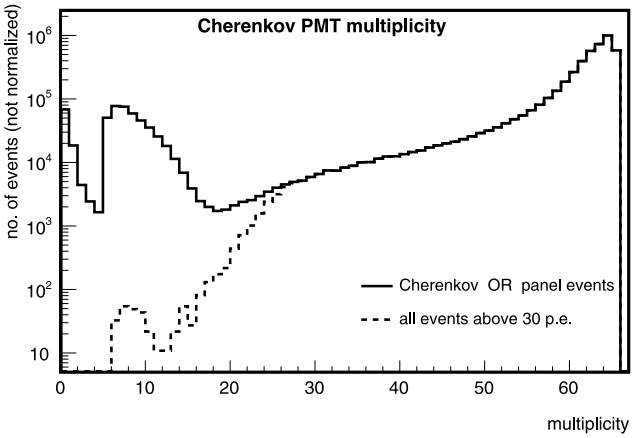

Fig. 19 Measured multiplicities of all mounted Cherenkov PMTs without cut on the number of detected photoelectrons (*full line*) and with a cut of ≥30 p.e. (*dashed line*)

from the water Cherenkov cannot contribute to $M < 5$. The increase close to $M = 0$ originates from triggers of the triple layered plastic scintillator when the muon hits the plastic but misses the water. Increasing the trigger threshold to 30 p.e. (dashed line) removes the intensity at low M.

The lower limit of the muon detection efficiency (MDE) is estimated for a threshold of 30 p.e. amounting to $\varepsilon_{\mathrm{md}} = (97.2 \pm 1.1)$ % [95]. MC estimates [90] give a value of $\varepsilon_{\mathrm{md}} = (99.1 \pm 0.4)$ %. The latter, however, includes an energy deposition of the muon within the full detector array. This selects automatically longer tracks within the water, which in turn produce more detectable light. The muon detection efficiency by the plastic detector alone amounts to $\varepsilon_{\mathrm{mpl}} = (95 \pm 8)$ %. The small geometrical coverage forbids the exclusive veto by the plastic only. A more refined determination employing coincidences between the plastic and Cherenkov detectors is under way.

Alternatively, one can estimate the efficiency that a muon detected in the Ge detector array is accompanied by a muon trigger. Two different event types were taken into account: (i) all events with >8.5 MeV deposited in germanium, but only one germanium detector fired; and (ii) all events with >4 MeV deposited in germanium, but at least two germanium detectors fired (α emitters from the U/Th decay chain have energy >4 MeV, but they would release their energy within one detector). In the commissioning runs, a total of 79 events were selected by these cuts, while 78 of them were also found in the muon veto. The muon "rejection efficiency" is calculated as $\varepsilon_{\mathrm{mr}} = (97.9^{+1.2}_{-2.0})$ % (median with 68 % central interval), which is in a good agreement with the simulations.

With the measured efficiency the background index due to un-identified prompt muons is estimated as $<10^{-5}$ cts/(keV kg yr), which is well below the specifications needed for Phase I and II [90].

7.2 Stability of Ge detectors

Initially, eight detectors from IGEX and HDM have been in operation in the GERDA cryostat. Two of them, ANG 1 and RG 3, developed high leakage currents at the beginning of Phase I. These detectors have been removed from the analysis of Phase I data. For some time however, they have been used as veto to suppress multi-site events. The remaining total mass for analysis is 14.6 kg with an average enrichment of 86 % in ^{76}Ge corresponding to 165 moles.

Energy calibrations are performed on a (bi)weekly basis with the ^{228}Th sources. Spectra of the six active enriched detectors are shown in Fig. 20, including scaled subplots for the 583.2 and the 2614.5 keV lines. The high count rates cause pile up that would manifest itself in tails on the low energy side of the peaks. Proper pile up rejection algorithms and further data quality cuts have been applied before the

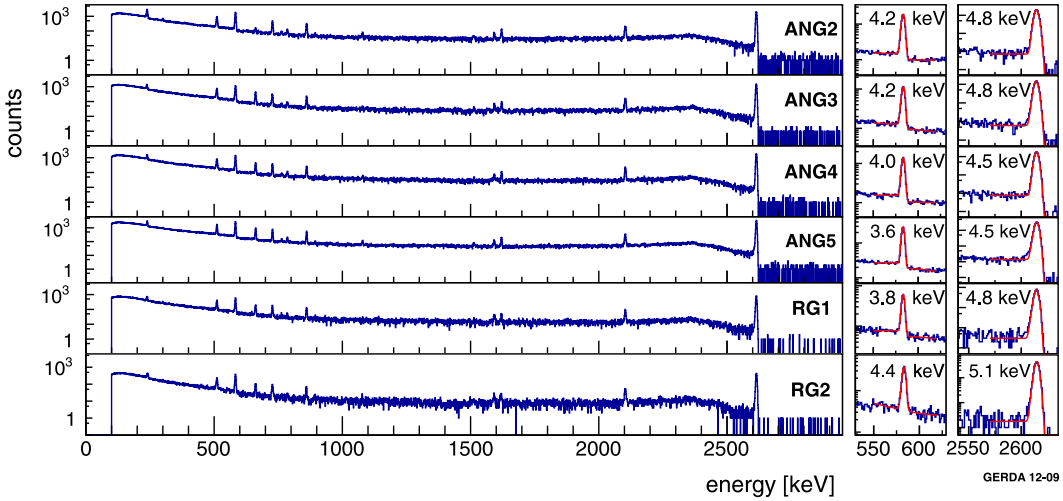

Fig. 20 The energy spectra of the six enriched germanium detectors are plotted for a calibration with ^{228}Th. The *blow-ups on the right* show the fit results for the 583.2 keV and the 2614.5 keV lines including the values for a Gaussian FWHM

fitting [112]. The peaks are fitted well by a Gaussian and an error function representing the background. The results are shown by the red lines and the FWHM of the Gaussian is given in keV. Values between 4.2 to 5.3 keV (FWHM) at 2614 keV have been obtained. These can be translated to a mass weighted average of 4.5 keV (FWHM) at $Q_{\beta\beta} = 2039.01(5)$ keV [131]. The resolution of the 2614.5 keV line for all detectors during the first months of data taking is shown in Fig. 21. No significant variation or trend is visible for this period.

The same is also true for the gain, which normally changed only after some power cycling or temperature drifts. The 2614.5 keV γ-line positions in the calibration spectra are stable in time as shown in Fig. 22 as they fall into a range of ± 1.3 keV. The shifts observed between two calibrations can be scaled linearly to the interesting energy at $Q_{\beta\beta}$. The two lines at ± 1.3 keV shown in Fig. 22 correspond to ± 1 keV at $Q_{\beta\beta}$. The gain shifts within the ROI thus are typically less than 1 keV. This value is small compared to the average FWHM of 4.5 keV and shows that the data from all periods can be added in the search for the peak of the $0\nu\beta\beta$ decay.

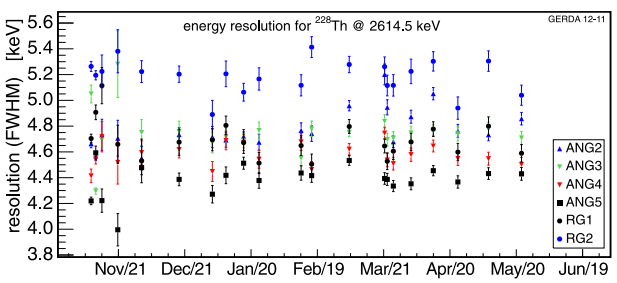

Fig. 21 The energy resolution of the germanium detectors is plotted for several energy calibrations with the ^{228}Th source

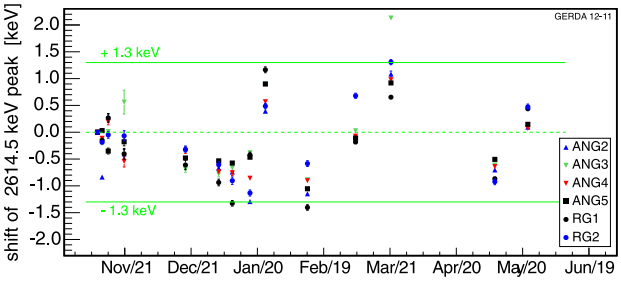

Fig. 22 Variations of the 2614.5 keV γ line between successive calibrations. The *green lines* indicate ± 1 keV variations at $Q_{\beta\beta}$ if scaled linearly in energy (Color figure online)

7.3 Background levels in GERDA

The commissioning of GERDA started with a string of three bare low background $^{\text{nat}}$Ge diodes, and yielded a surprisingly large BI on the order of the HDM and IGEX experiments ($18 \cdot 10^{-2}$ cts/(keV kg yr), see Table 7). As another surprise, the line at 1525 keV from ^{42}K, the daughter of ^{42}Ar, appeared in the spectra with an intensity much higher than expected on the basis of the upper limit for the ratio ^{42}Ar/$^{\text{nat}}$Ar determined by V.D. Ashitkov et al. [132]. The published limit of $<4.3 \times 10^{-21}$ g/g at 90 % confidence level converts to an upper limit of 41 µBq/kg for ^{42}Ar. These observations led to the working hypothesis that charged ions, and in particular the progeny ^{42}K, are drifting in the electric field of the bare Ge diodes that are biased with 3 to 4 kV via the large n^+ surface (see Sect. 3 and Fig. 2). The concentration of radioactive impurities near the Ge diodes can increase. Further studies with different bias schemes confirmed this hypothesis. A major improvement of the BI was achieved by enclosing the string of detectors with a cylinder, made of 60 µm thick Cu foil, called "mini-shroud"

Table 7 The background index deduced (without pulse shape analysis) from the event count in the indicated energy windows ΔE for different running conditions during the commissioning and the first part of Phase I. Corresponding values are shown also for the IGEX and HDM experiments

experiment diode environment	diodes	ΔE (keV)	exposure (kg yr)	background index 10^{-2} cts/(keV kg yr)
IGEX [30–33]				
vacuum, Cu enclosed	enr	2000–2500	4.7	26
HDM [62]				
vacuum, Cu enclosed	enr	2000–2100	56.7	16
GERDA commissioning				
LAr	nat	1839–2239	0.6	18 ± 3
LAr, Cu mini-shroud	nat	1839–2239	2.6	5.9 ± 0.7
ditto	enr	1839–2239	0.7	$4.3^{+1.4}_{-1.2}$
GERDA Phase I				
LAr, Cu mini-shroud	nat	1839–2239*	1.2	$3.5^{+1.0}_{-0.9}$
LAr (diodes AC-coupled)	nat	1839–2239*	1.9	$6.0^{+1.0}_{-0.9}$
LAr, Cu mini-shroud	enr	1939–2139*	6.1	$2.0^{+0.6}_{-0.4}$

*Excluding the blinded region of $Q_{\beta\beta} \pm 20$ keV

(BI $\approx 5.9 \cdot 10^{-2}$ cts/(keV kg yr)). The volume of LAr from which the ions can be collected onto the surface of the detectors is reduced and bulk convection of the LAr near the detectors is prevented. In fact, operating the Ge diodes in AC-coupled mode (n^+ surface grounded and p^+ contact biased) without mini-shroud but with adequate shielding of the p^+ contact, i.e. without external electrical stray field, yielded a similar BI of $6.0 \cdot 10^{-2}$ cts/(keV kg yr) (see next to last line in Table 7). For the Phase I physics run, the hermeticity of the mini-shroud, as well as the shielding of the HV cables, was further improved in order to avoid any leakage of electric field lines into the LAr volume. The improvement with respect to the precursor experiments is evident. The stability of the BI must be proven for a longer period of time.

An analysis of the intensity of the 1525 keV line gives a concentration for ^{42}Ar that is about twice the literature limit. This estimate is based on the assumption of a homogeneous distribution of this isotope outside the mini-shroud.

The intensity of γ lines was investigated in order to identify sources of backgrounds. The results are compiled in Table 8 for the natural and the enriched detectors in comparison to numbers from HDM [60]. The rate estimates are based on a Bayesian approach starting with a flat prior probability distribution function. The general observation is an achieved reduction by about a factor of 10 with respect to

Table 8 Counts and rates of background lines for the enriched and natural detectors in GERDA in comparison to the enriched detectors of HDM [60]. Upper limits correspond to 90 % credibility interval. The central value is the mode of the posterior probability distribution function and the error bars account for the smallest interval containing 68 % probability

isotope	energy [keV]	^{nat}Ge (3.17 kg yr)		^{enr}Ge (6.10 kg yr)		HDM (71.7 kg yr)
		tot/bck [cts]	rate [cts/(kg yr)]	tot/bck [cts]	rate [cts/(kg yr)]	rate [cts/(kg yr)]
^{40}K	1460.8	85/15	$21.7^{+3.4}_{-3.0}$	125/42	$13.5^{+2.2}_{-2.1}$	181 ± 2
^{60}Co	1173.2	43/38	<5.8	182/152	$4.8^{+2.8}_{-2.8}$	55 ± 1
	1332.3	31/33	<3.8	93/101	<3.1	51 ± 1
^{137}Cs	661.6	46/62	<3.2	335/348	<5.9	282 ± 2
^{228}Ac	910.8	54/38	$5.1^{+2.8}_{-2.9}$	294/303	<5.8	29.8 ± 1.6
	968.9	64/42	$6.9^{+3.2}_{-3.2}$	247/230	$2.7^{+2.8}_{-2.5}$	17.6 ± 1.1
^{208}Tl	583.2	56/51	<6.5	333/327	<7.6	36 ± 3
	2614.5	9/2	$2.1^{+1.1}_{-1.1}$	10/0	$1.5^{+0.6}_{-0.5}$	16.5 ± 0.5
^{214}Pb	352	740/630	$34.1^{+12.4}_{-11.0}$	1770/1688	$12.5^{+9.5}_{-7.7}$	138.7 ± 4.8
^{214}Bi	609.3	99/51	$15.1^{+3.9}_{-3.9}$	351/311	$6.8^{+3.7}_{-4.1}$	105 ± 1
	1120.3	71/44	$8.4^{+3.5}_{-3.3}$	194/186	<6.1	26.9 ± 1.2
	1764.5	23/5	$5.4^{+1.9}_{-1.5}$	24/1	$3.6^{+0.9}_{-0.8}$	30.7 ± 0.7
	2204.2	5/2	$0.8^{+0.8}_{-0.7}$	6/3	$0.4^{+0.4}_{-0.4}$	8.1 ± 0.5

the HDM experiment. The composition of the background in relation to the screening results will be discussed in a future publication.

Additional contributions to the BI will result from radioactive surface contaminations such as ^{210}Pb as well as from cosmogenically produced radioisotopes within the diodes. These contributions are expected to be small and will require large data sets to evaluate.

Finally, it is worth to mention that auxiliary experiments were performed to study the cross sections of cosmogenic activation of steel and other constructional materials [133], the inelastic neutron scattering [134], the neutron activation cross sections, and the γ decay spectra [135–139]. The deduced contributions to the BI are in the order of few 10^{-5} cts/(keV kg yr).

First energy spectra for enriched and natural diodes are shown in Fig. 23. Notice, that the spectrum from the natural detectors has been renormalized to match the exposure of the enriched diodes. The low energy part is dominated by the β decay of ^{39}Ar which has an endpoint energy of 565 keV. The well known activity of $A(^{39}\mathrm{Ar}) = [1.01 \pm 0.02(\mathrm{stat}) \pm 0.08(\mathrm{syst})]$ Bq/kg (Ref. [140]) describes the observed intensity. The enhancement of $2\nu\beta\beta$ events in the range from 600 to 1400 keV for the enriched detectors is clearly visible.

The BI of $(2.0^{+0.6}_{-0.4}) \cdot 10^{-2}$ cts/(keV kg yr) for the enriched detectors is evaluated in the energy region $Q_{\beta\beta} \pm 100$ keV with the 2019 to 2059 keV window excluded (green bar in Fig. 23). This value is an order of magnitude lower than the one for the very same detectors in their previous shielding in the HDM and IGEX experiments (see Table 7).

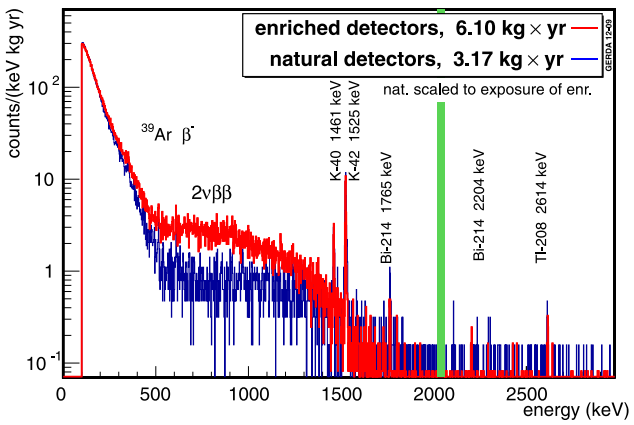

Fig. 23 Spectra taken with enriched (*red*) and non-enriched (*blue*) detectors during the same time period. The $^{\mathrm{nat}}$Ge spectrum has been normalized to match the exposure of $^{\mathrm{enr}}$Ge. The blinding window of $Q_{\beta\beta} \pm 20$ keV is indicated as *green bar*. Identified γ lines are indicated (Color figure online)

8 Conclusions

GERDA searches for $0\nu\beta\beta$ decay of ^{76}Ge using a new experimental concept. Bare germanium diodes are operated successfully in a 4 m diameter cryostat filled with LAr, requiring only a small amount of radiopure materials as mechanical and electrical support. Shielding against external background is achieved by LAr and an additional shell of 3 m of water.

The experiment started commissioning in May 2010 and in November 2011 with physics data taking (Phase I). The experience gained so far shows that all components work well.

1. The operation of the cryostat inside the water tank is stable and safe.
2. Bare germanium diodes are operated reliably in liquid argon over a long time and the implemented handling procedure ensures that many operational cycles do not deteriorate the performance.
3. The readout electronics is balancing the partially conflicting requirements of good energy resolution, low radioactivity, and operation at LAr temperature.
4. The water tank instrumentation ensures a high veto efficiency of muon events and only a tolerable loss of 3 out of 66 PMTs have stopped functioning during a 2 year period.
5. Data acquisition and monitoring of the ambient parameters operate reliably.
6. The implemented software allows for a fast reconstruction of the data together with a good monitoring of data quality.

The experience from the (bi-)weekly calibrations shows that the gain drifts of the entire readout chain are typically smaller than 1 keV at $Q_{\beta\beta}$. This is small enough to ensure that adding all data will not result in relevant shifts of peak positions or deteriorations of resolutions.

The surprisingly large background from ^{42}K, the ^{42}Ar progeny, experienced during the commissioning can be mitigated by two methods: encapsulation of each detector string by a closed thin-walled copper cylinder or AC coupling of the detectors. In both cases the electric field outside of the encapsulation is minimized.

The Phase I background is determined currently to $(2.0^{+0.6}_{-0.4}) \cdot 10^{-2}$ cts/(keV kg yr). This value and the intensities of gamma lines show an order of magnitude improvement compared to the previous HDM and IGEX experiments. In the absence of a signal and given the current BI, GERDA expects to set 90 % probability lower limits of $T_{1/2} > 1.9 \cdot 10^{25}$ yr for an exposure of 20 kg yr.

Acknowledgements The GERDA experiment is supported financially by the German Federal Ministry for Education and Research (BMBF), the German Research Foundation (DFG) via the Excellence

Cluster Universe, the Italian Istituto Nazionale di Fisica Nucleare (INFN), the Max Planck Society (MPG), the Polish National Science Centre (NCN), the Russian Foundation for Basic Research (RFBR), and the Swiss National Science Foundation (SNF). The institutions acknowledge also internal financial support.

The GERDA collaboration thanks the directors and the staff of the LNGS for their continuous strong support of the GERDA experiment.

Preparing and setting up the infrastructure of the GERDA experiment was made possible only through the indispensable help of R. Adinolfi Falcone, T. Apfel, P. Aprili, J. Baumgart, G. Bucciarelli, M. Castagna, F. Costa, N. D'Ambrosio, S. Flicker, D. Franciotti, H. Fuchs, H. Hess, V. Mallinger, P. Martella, B. Mörk, D. Orlandi, M. Reissfelder, T. Schwab, R. Sedlmeyr, S. Stalio, R. Tartaglia, E. Tatananni, M. Tobia, D. Wamsler, G. Winkelmüller, and T. Weber.

The prolific cooperation with P. Vermeulen and J. Verplancke from Canberra SNV, Olen in the context of refurbishment of the enriched germanium diodes is appreciated.

Open Access This article is distributed under the terms of the Creative Commons Attribution License which permits any use, distribution, and reproduction in any medium, provided the original author(s) and the source are credited.

References

1. I. Abt et al. (GERDA Collaboration), GERDA: The GERmanium Detector Array for the search of neutrinoless $\beta\beta$ decays of ^{76}Ge at LNGS, Letter of Intent to LNGS, see also: 0404.0390 [hep-ex], Proposal to LNGS 38/04 (2004), http://www.mpi-hd.mpg.de/gerda/; PhD theses: http://www.mpi-hd.mpg.de/gerda/public/phd.html
2. J. Schechter, J.W.F. Valle, Phys. Rev. D **25**, 2951 (1982)
3. S. Davidson, E. Nardi, Y. Nir, Phys. Rep. **466**, 105 (2008)
4. F. Avignone III, S.R. Elliot, J. Engel, Rev. Mod. Phys. **80**, 481 (2008)
5. A.S. Barabash, Phys. At. Nucl. **74**, 603 (2011)
6. J.J. Gomez-Cadenas et al., Riv. Nuovo Cimento **35**, 29 (2012)
7. S.R. Elliot, Mod. Phys. Lett. A **27**, 1230009 (2012)
8. B. Schwingenheuer, in *Procs. 12th International Conference on Topics in Astroparticle and Underground Physics*, Munich, Sep. 5–9 (2011)
9. M. Doi, T. Kotani, E. Takasugi, Prog. Theor. Phys. Suppl. **83**, 1 (1985)
10. J. Suhonen, O. Civitarese, Nucl. Phys. A **847**, 207 (2010), and refs. therein
11. J. Suhonen, Inst. Phys. Conf. Ser. **375**, 042026 (2012)
12. J. Menendez, A. Poves, E. Caurier, F. Nowacki, Nucl. Phys. A **818**, 139 (2009), and refs. therein
13. V.A. Rodin et al., Nucl. Phys. A **766**, 107 (2006) [Erratum-Ibid. A **793**, 213 (2007)]
14. F. Simkovic et al., Phys. Rev. C **79**, 055501 (2009)
15. V.A. Rodin, Inst. Phys. Conf. Ser. **375**, 042025 (2012)
16. J. Barea, F. Iachello, Phys. Rev. C **79**, 044301 (2009)
17. W. Rodejohann, Int. J. Mod. Phys. E **20**, 1833 (2011)
18. E. Fiorini et al., Phys. Lett. B **25**, 602 (1967)
19. F.T. Avignone III et al., Phys. Rev. Lett. **50**, 721 (1983)
20. J.J. Simpson et al., Phys. Rev. Lett. **53**, 141 (1984)
21. E. Bellotti et al., Phys. Lett. B **146**, 450 (1984)
22. H. Ejiri et al., Nucl. Phys. A **448**, 271 (1986)
23. D. Caldwell, J. Phys. G **17**, S137 (1991)
24. P. Fisher et al., Phys. Lett. B **218**, 257 (1989)
25. A. Morales et al., J. Phys. G **17**, S211 (1991)
26. J. Busto et al., Nucl. Phys. A **513**, 291 (1990)
27. A.A. Vasenko et al., Mod. Phys. Lett. A **5**, 1299 (1990)
28. I.V. Kirpichnikov, Preprint ITEP91-91, 1991
29. H.V. Klapdor-Kleingrothaus et al. (HDM-Collaboration), Eur. Phys. J. A **12**, 147 (2001)
30. C.E. Aalseth et al. (IGEX-Collaboration), Phys. Rev. D **65**, 092007 (2002)
31. C.E. Aalseth et al., Phys. Rev. C **59**, 2108 (1999)
32. D. Gonzalez et al., Nucl. Phys. B, Proc. Suppl. **87**, 278 (2000)
33. D. Gonzalez et al., Nucl. Instrum. Methods A **515**, 634 (2003)
34. H.V. Klapdor-Kleingrothaus et al., Phys. Lett. B **586**, 198 (2004)
35. R. Henning (MAJORANA-Collaboration), AIP Conf. Proc. **1182**, 88 (2009)
36. J. Wilkerson et al., Inst. Phys. Conf. Ser. **375**, 042010 (2012)
37. G. Heusser, Annu. Rev. Nucl. Part. Sci. **45**, 543 (1995)
38. A. Smolnikov, P. Grabmayr, Phys. Rev. C **81**, 028502 (2010)
39. Yu.G. Zdesenko et al., J. Phys. G, Nucl. Part. Phys. **27**, 2129 (2001)
40. M. Di Marco, P. Peiffer, S. Schönert, Nucl. Phys. Proc. Suppl. **172**, 45 (2007)
41. P. Peiffer et al., J. Instrum. **3**, P08007 (2008)
42. 8″ PMT, type 9357, 9350KB & KB9354KB. ET Enterprises Limited, Uxbridge, UK
43. M. Agostini et al., Inst. Phys. Conf. Ser. **375**, 042009 (2012)
44. H. Neder, G. Heusser, M. Laubenstein, Appl. Radiat. Isot. **53**, 191 (2000)
45. L. Baudis et al., J. Instrum. **6**, P08010 (2011)
46. S. Agostinelli et al. (Geant4 Collaboration), Nucl. Instrum. Methods A **506**, 250 (2003)
47. J. Allison et al. (Geant4 Collaboration), IEEE Trans. Nucl. Sci. **53**, 270 (2006)
48. M. Boswell et al., IEEE Trans. Nucl. Sci. **58**, 1212 (2011). arXiv:1011.3827 [nucl-ex]
49. I. Barabanov et al., Nucl. Instrum. Methods A **606**, 790 (2009)
50. A.V. Dementyev, N.M. Sobolevsky, Radiat. Meas. **30**, 553 (1999)
51. I. Barabanov et al., Nucl. Instrum. Methods B **251**, 115 (2006)
52. W.B. Wilson et al., SOURCES-4A, Technical Report LA-441 13539-MS Los ALamos, 1999
53. M. Agostini et al., Nucl. Phys. B, Proc. Suppl. **229–232**, 489 (2012)
54. Canberra Semiconductor, NV, Lammerdries 25, B-2250, Olen, Belgium
55. M. Barnabé Heider et al., Procs. NSS08, IEEE Conf. publication 3513, 2008
56. M. Barnabé Heider, PhD thesis, U. Heidelberg, May 2009
57. H.V. Klapdor-Kleingrothaus, Nucl. Instrum. Methods A **566**, 472 (2006)
58. J. Hellmig, H.V. Klapdor-Kleingrothaus, Z. Phys. A **359**, 351 (1997)
59. L. Baudis et al., Nucl. Instrum. Methods A **481**, 149 (2002)
60. O. Chkvorets, PhD Thesis, U. Heidelberg, 2008
61. High Activity Disposal Experimental Site (HADES) of the Belgian Nuclear Research Center SCK·CEN, Boeretang 200, BE-2400 Mol, Belgium
62. H.V. Klapdor-Kleingrothaus et al., Nucl. Instrum. Methods A **522**, 371 (2004)
63. V. Khournoukov, priv. communication; measurements performed by the Botchvar Insitute, Moscow, Russia
64. J.R. De Laeter et al., Pure Appl. Chem. **75**, 683 (2003)
65. M. Barnabé Heider et al., J. Instrum. **5**, P10007 (2010)
66. Currently known as Joint Stock Company "Production Association Electrochemical Plant" (JSC "PA Electrochemical Plant"), uranium enrichment enterprise of the State Atomic Energy Corporation "Rosatom"
67. PPM Pure Metals, GmbH, in Langelsheim, Germany
68. Canberra Oak Ridge, USA
69. E. Haller, Adv. Phys. **30**, 93 (1981)

70. CANBERRA Broad Energy Ge (BEGe) Detector, www.canberra.com/products/485.asp
71. D. Budjáš et al., J. Instrum. **4**, P10007 (2009)
72. M. Agostini et al., J. Instrum. **6**, P03005 (2011)
73. K. Zuber, PhD thesis, U. Heidelberg, 1992; analysis of ANG 1 by J. Echternach
74. F.T. Avignone, priv. comm., 2011
75. W. Maneschg et al., Nucl. Instrum. Methods A **593**, 448 (2008)
76. Torlon type 4503, Torlon is a trademark of Solvay Advanced Polymers
77. G. Heusser et al., Appl. Radiat. Isot. **52**, 691 (2000)
78. Synthetic charcoal by Carbo-Act International (NL)
79. Makrolon is a registered trade mark of BASF
80. Ch. Haberstroh, Adv. Cryog. Eng. **53**, 1201 (2008)
81. LD301 HART Pressure Transmitter, SMAR Research Corporation, NY, USA
82. M. Balata et al., Nucl. Instrum. Methods A **370**, 605 (1996)
83. M.G. Giammarchi et al., Ultrapure Water **13**, 59 (1996)
84. Institute of Environmental Science and Technology, Arlington Heights (IL), USA
85. Habia cable, Upplands Väsby, Sweden
86. Sami S.p.a, Liscate (MI) Italy
87. Teledyne Reynolds UK, Newbury, Berkshire, UK
88. F. Froborg, PhD thesis, U. Zurich, 2012
89. National Instruments Corporation, Austin (TX), USA
90. M. Knapp, PhD thesis, Kepler Center for Astro and Particle Physics, U. Tübingen, 2009
91. Daylighting Film DF2000MA (VM2000), 3M, St. Paul, MN, USA
92. RG213C/U by JOWO Systemtechnik, Delmenhorst, Germany
93. CAEN S.p.A., Viareggio, Italy
94. F. Ritter et al., Nucl. Instrum. Methods A **617**, 420 (2010)
95. F. Ritter, PhD thesis, Kepler Center for Astro and Particle Physics, U. Tübingen, 2012
96. Scintillator UPS-923A is based on polystyrol with additive of PTP (2 %) and POPOP (0.03 %) built by the Kharkov Crystal Institute, Ukraine
97. HM6780-2 (Ø 8 mm) Hamamatsu Photonics K.K., Hamamatsu City, Japan
98. PMT-85 (Ø 30 mm) by Kvadrotech, Moscow, RU
99. S-type Y11(250)M, Kuraray, Japan. (The middle of the fiber is made of polystyrol with additive 0.02 % of wavelength shifter Y11. The internal part of fiber consists of PMMA, external from the fluorinated PMMA)
100. S. Riboldi et al., in *Procs. IEEE Nuclear Science Symposium and Int. Workshop on Room Temperature Semiconductor Detectors*, Oct. 30–Nov. 6 (2010), p. 1386
101. Polyflon Company, One Willard Road, Norwalk, CT 06851, USA
102. Stycast, Emerson & Cuming, Westerlo, Belgium
103. R. Isocrate et al., LNL Annual Report 2004, 226
104. C.A. Ur et al., LNL Annual Report 2004, 228
105. J. Stein, F. Scheuer, W. Gast, A. Georgiev, Nucl. Instrum. Methods B **113**, 141 (1996)
106. Qt cross platform application frame work, Qt Project Hosting, Oslo, Norway
107. STRUCK Innovative Systeme GmbH, 22399 Hamburg, Germany
108. PAS9817/AO DAC, Precision Analog Systems Co., Plantation (FL) USA
109. M. Agostini et al., Inst. Phys. Conf. Ser. **375**, 042027 (2012)
110. R. Brun, F. Rademakers, Nucl. Instrum. Methods A **389**, 81 (1997)
111. M. Agostini, L. Pandola, P. Zavarise, O. Volynets, J. Instrum. **6**, P08013 (2011)
112. M. Agostini, L. Pandola, P. Zavarise, Inst. Phys. Conf. Ser. **368**, 012047 (2012)
113. P. Zavarise et al., Inst. Phys. Conf. Ser. **375**, 042028 (2012)
114. Hewlett Packard ProCurve Switch 2810-48G
115. DELL Power Edge R300, Quad Core Xeon X3323, 2.5 GHz
116. R. Brugnera et al., J. Instrum. **7**, P100712 (2012)
117. PostgreSQL Database Management System
118. Ajax (Asynchronous JavaScript and XML), J.J. Garrett, Ajax: A New Approach to Web Applications, Adaptive Path 2005
119. H. Neder et al., Appl. Radiat. Isot. **53**, 191 (2000)
120. G. Heusser et al., in *Procs. International Conference on Isotopes in Environmental Studies*, ed. by P.P. Povinec, J.A. Sanchez-Cabeza (Elsevier, Amsterdam, 2006), p. 495
121. R. Wink et al., Nucl. Instrum. Methods A **329**, 541 (1993)
122. D. Budjáš et al., Appl. Radiat. Isot. **67**, 755 (2009). The numbers quoted in Table 1 have been obtained by using the simulations as described in I. Abt et al., AIP Conf. Proc. **897**, 9 (2007). Numbers in Table 1 are courtesy of K. Kroeninger and X. Liu
123. G. Zuzel, H. Simgen, Appl. Radiat. Isot. **67**, 889 (2009)
124. G. Heusser et al., Appl. Radiat. Isot. **52**, 691 (2000)
125. H. Simgen, G. Zuzel, Appl. Radiat. Isot. **67**, 922 (2009)
126. C. Arpesella et al. (BOREXINO Collaboration), Astropart. Phys. **18**, 1 (2002)
127. DuPont Performance Elastomers, Wilmington (DE), USA, or Ethylen-Propylen-Dien-Monomer (EPDM)
128. Pfeiffer Vakuum, Asslar, Germany
129. BD Sensors, Thierstein, Germany
130. B. Bellini et al., J. Cosmol. Astropart. Phys. **5**, 015 (2012)
131. G. Douysset et al., Phys. Rev. Lett. **86**, 4259 (2001)
132. V.D. Ashitkov et al., Instrum. Exp. Tech. **46**, 153–160 (2003)
133. M. Laubenstein, G. Heusser, Appl. Radiat. Isot. **67**, 750 (2009)
134. A. Domula, PhD thesis in preparation, TU Dresden
135. G. Meierhofer et al., Phys. Rev. C **81**, 027603 (2010)
136. G. Meierhofer et al., Eur. Phys. J. A **40**, 61 (2009)
137. J. Marganiec et al., Phys. Rev. C **79**, 065802 (2009)
138. J. Marganiec et al., J. Phys. G **35**, 014022 (2008)
139. G. Meierhofer et al., Eur. Phys. J. A **48**, 20 (2012)
140. P. Benetti et al., Nucl. Instrum. Methods A **574**, 83 (2007)